Dissertations, Master's Theses and Master's Reports - Open

Dissertations, Master's Theses and Master's Reports

2011

Detection of complex point targets with distributed assets in a MIMO radar system

Ishtiaque Amin
Michigan Technological University

Follow this and additional works at: https://digitalcommons.mtu.edu/etds

Part of the Electrical and Computer Engineering Commons

Recommended Citation

Amin, Ishtiaque, "Detection of complex point targets with distributed assets in a MIMO radar system", Master's report, Michigan Technological University, 2011.
https://digitalcommons.mtu.edu/etds/575

DETECTION OF COMPLEX POINT TARGETS

WITH DISTRIBUTED ASSETS IN A MIMO RADAR SYSTEM

By

ISHTIAQUE AMIN

A REPORT

Submitted in partial fulfillment of the requirements for the degree of

MASTER OF SCIENCE

ELECTRICAL ENGINEERING

MICHIGAN TECHNOLOGICAL UNIVERSITY

2011

This report "Detection of Complex Point Targets with Distributed Assets in a MIMO Radar System," is hereby approved in partial fulfillment of the requirements for the Degree of MASTER OF SCIENCE in Electrical Engineering.

DEPARTMENT:

Electrical and Computer Engineering

Signatures:

Report Advisor   _____

Dr. Daniel Fuhrmann

Committee Member   _____

Dr. Zhijun Zhao

Committee Member   _____

Dr. Renfang Jiang

Department Chair   _____

Dr. Daniel Fuhrmann

Date   _____

To Mom, Dad, Sister and everyone back home

&

My Advisor, Dr. Daniel Fuhrmann

Brief Content

Contents

Acknowledgements

List of Figures

Abstract

The report explores the problem of detecting complex point target models in a MIMO radar system. A complex point target is a mathematical and statistical model for a radar target that is not resolved in space, but exhibits varying complex reflectivity across the different bistatic view angles. The complex reflectivity can be modeled as a complex stochastic process whose index set is the set of all the bistatic view angles, and the parameters of the stochastic process follow from an analysis of a target model comprising a number of ideal point scatterers randomly located within some radius of the targets center of mass. The proposed complex point targets may be applicable to statistical inference in multistatic or MIMO radar system.

Six different target models are summarized here – three 2-dimensional (Gaussian, Uniform Square, and Uniform Circle) and three 3-dimensional (Gaussian, Uniform Cube, and Uniform Sphere). They are assumed to have different distributions on the location of the point scatterers within the target.

We develop data models for the received signals from such targets in the MIMO radar system with distributed assets and partially correlated signals, and consider the resulting detection problem which reduces to the familiar Gauss-Gauss detection problem. We illustrate that the target parameter and transmit signal have an influence on the detector performance through target extent and the SNR respectively. A series of the receiver operator characteristic (ROC) curves are generated to notice the impact on the detector for varying SNR. Kullback–Leibler (KL) divergence is applied to obtain the approximate mean difference between density functions the scatterers assume inside the target models to show the change in the performance of the detector with target extent of the point scatterers.

Keywords: MIMO radar, target model, target extent, SNR, ROC, KL divergence.

Chapter 1 ~ Introduction

RADAR theory has been a vibrant scientific field for the last few decades. It deals with many different diverse problems. However, one of the most important problems is the detection of a target in a given 3-dimensional space. The importance of this problem is not limited to radars, and other engineering disciplines like sonar and communication deal with very similar problems. In the recent years, radar systems have developed considerably that can be attributed to the increase in computation power and advances in hardware design. While early radar systems utilized a directional antenna, modern day radar systems can synthesize the beams and simultaneously scan a given space. Radar systems come in different flavors, and here we will focus on the multiple-input multiple-output (MIMO) radar system.

MIMO radar and multistatic radar systems have received considerable theoretical interest in recent years (1). It consists of an architecture that employs assets, in the form of transmitter and receiver antennas, to emit orthogonal or non-coherent waveforms. Two forms of such radar system are generally studied: MIMO radars with widely separated antennas, and the MIMO radars with collocated antennas (8,19). Both have many unique advantages, but both also face many challenges. Fishler *et al.* were the first to point out that MIMO radar system with widely separated antennas provides the important feature of spatial diversity that exploits the radar cross-section (RCS) diversity (2,27-28). When the orthogonal components are transmitted from different antennas, each orthogonal waveform will carry independent information about the target (26). This phenomenon can be utilized to devise a better performing detector. MIMO radar with collocated assets can exploit the waveform diversity. This is important as it can significantly improve system identification, increase target detection and parameter estimation, and enhance transmit beam pattern design.

In this report we examine the spatially distributed assets case in a multistatic radar environment, where the transmit/receive antennas are positioned widely apart, and the transmitters emit orthogonal signals. We assume that each transmitter/receiver module

transmits different signal modulation on the common carrier, all receivers respond to all signals, and carriers are phase-synchronous. Different target models have been examined, with different distributions, and the resulting detection problem has been devised. We then proceed to identify the parameters that have an influence on the performance of target detection.
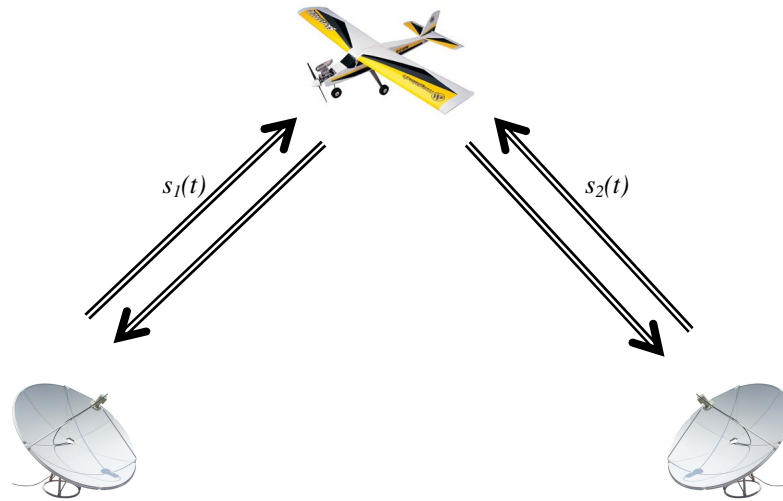
Figure 1.1: Spatial Diversity MIMO Radar

In the following chapters we will examine the complex point targets in light of recent interest in MIMO and multistatic radar systems. Complex reflectivity has been characterized as a stochastic process in (7) defined on the space of pairs of the transmitter and the receiver view angles. The target model itself consists of a finite number of ideal point scatterers randomly located at given positions from the center of mass of the target (3-5). Depending on the distribution on scatterer location, we have obtained closed-form expressions for the correlation functions between two bistatic views. The key idea here is that the target appears different from different view angles.

This report is organized as follows. In Chapter 2, we analyze six different target models – three in 2 dimensions (Gaussian, Uniform Square, and Uniform Cube) and three in 3 dimensions (Gaussian, Uniform Cube, and Uniform Sphere). We depict a synopsis of these target models in the MATLAB GUI-based simulation tools that has been designed by John Vander Laan. All of these models lead to similar qualitative results, shown in

Chapter 3 and Appendix A, and depend on the spatial extent of the target (normalized by the wavelength, λ). We then incorporate these models into the familiar Gauss-Gauss detection problem for a MIMO radar system with distributed assets (*i.e.* varying the bistatic view angles on target by means of 4 transmitters, and 4 receivers), and generate histogram plots for two hypotheses (noise only, and signal+noise) in Chapter 3.

In Chapter 4, we identify two parameters that have an effect on the performance of the detector. They are – transmitted signal-to-noise ratio (SNR), and the spatial extent of the target, in terms of wavelength, λ. For the first case, we keep the target's spatial extent fixed and vary SNR of the transmitted signal to generate a series of the receiver operator characteristic (ROC) curves. This process is then reversed, and we look at the performance by altering the target's spatial extent, keeping SNR fixed. For either case, the Kullback-Leibler (KL) divergence is introduced to provide additional support to the claim that transmitted signal SNR and spatial extents of the targets impact the detector performance (in Chapter 4, and Appendix B & C).

Chapter 2 ~ Target Models

2.1 Common Target Model

In this chapter we look at the target models for the detection problem. All these models have been derived in (7). A *complex point target* is a reflected target that is not resolved in space by radar waveform, but exhibits a different radar cross-section or complex reflectivity as a function of bistatic view angle, which means that it appears to occupy a single point in space or one range resolution cell, as the spatial extent is less than *c/2B* where *c* is the speed of light, and *B* is the radar signal bandwidth. The complex point target's radar cross-section (RCS) or the complex reflectivity is a stochastic process whose index set is the set of all the bistatic view angles. The parameters of this stochastic process follow from an analysis of a target model.
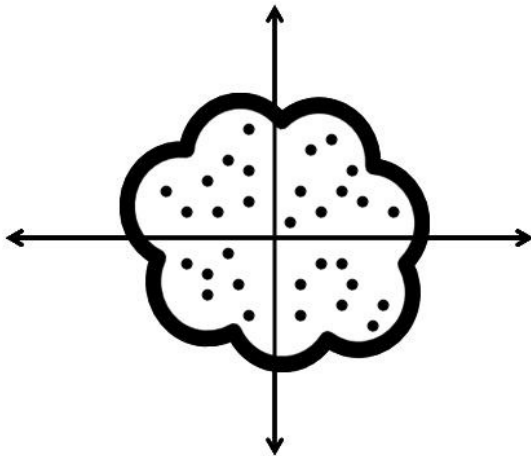
Figure 2.1: Multiple Point Scatterer Model Figure 2.2: Unit Vectors to Transmitter & Receiver
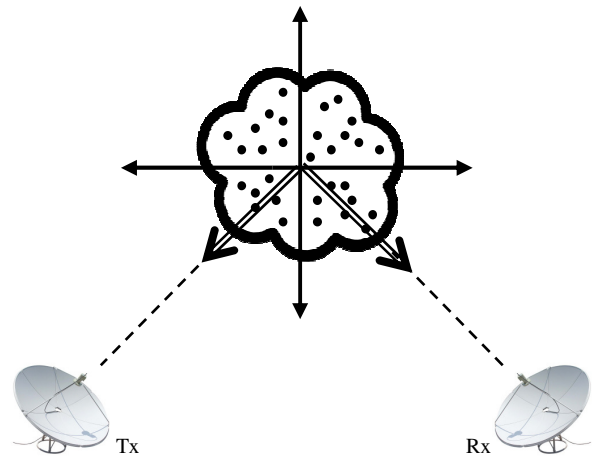
A target model is assumed to consist of a collection of discrete isotropic point scatterers that are randomly located at positions **x**, around the center of mass of the target. We say that each of these point scatterer, shown as black dots in Figures 2.1 and 2.2, in the target model exhibits a complex reflectivity ρ that assumes distribution of $CN(0, \sigma^2)$ with zero mean, and a given variance. Let *L* be the total path length from transmitter to the scatterer, and then from the scatterer to the transmitter. The target is assumed to be at the center of the coordinate axes. The differential path length ΔL, relative to the path

length obtained with the exact same scatterer located at the origin of a coordinate axes, becomes as follows

$$\Delta L \;=\; \mathbf{u}_T^{\mathrm{T}}\mathbf{x} + \mathbf{u}_R^{\mathrm{T}}\mathbf{x} \;=\; (\mathbf{u}_T + \mathbf{u}_R)^{\mathrm{T}}\,\mathbf{x} \tag{2.1}$$

where , $\mathbf{u}_T$ and $\mathbf{u}_R$ are unit vectors pointing in the direction towards the transmitter and the receiver respectively shown in Figure 2.3. This generates a differential time delay of

$$\Delta\tau = \frac{\Delta L}{c} \tag{2.2}$$

This can be translated into a phase shift, where the phase term is given by

$$h \;=\; e^{j2\pi f_c \Delta\tau} \;=\; e^{\frac{j2\pi(\mathbf{u}_T + \mathbf{u}_R)^{\mathrm{T}}\mathbf{x}}{\lambda}} \tag{2.3}$$

where λ is the carrier wavelength. Since h depends on the random location of $\mathbf{x}$, it is a random variable.

The complex reflectivity of the target becomes a function of the pair $(\mathbf{u}_T,\ \mathbf{u}_R)$ which is referred to collectively as the *bistatic view angle*. The function $\rho(\mathbf{u}_T,\ \mathbf{u}_R)$ is a *stochastic process* whose index set is a set of all the bistatic view angles and whose range is $\mathbb{C}$. Its randomness comes from distribution on the scatterer location $\mathbf{x}$.

$$\rho : S^1 \times S^1 \to \mathbb{C} \tag{2.4}$$

in two dimensions, and in three dimensions we have

$$\rho : S^2 \times S^2 \to \mathbb{C} \tag{2.5}$$

where S^1 and S^2 are unit circle and unit sphere respectively. The conditional distribution of $\rho(\mathbf{u}_{T2},\ \mathbf{u}_{R2})$ given $\rho(\mathbf{u}_{T1},\ \mathbf{u}_{R1})$ is concentrated on a circle in $\mathbb{C}$.

2.2 Specific Target Model

Let us assume that $(\mathbf{u}_{T1},\ \mathbf{u}_{R1})$ and $(\mathbf{u}_{T2},\ \mathbf{u}_{R2})$ are a pair of bistatic view angles. If ρ is a function of this pair of bistatic view angle, we can model ρ as a stochastic process given by $\rho(\mathbf{u}_{T1},\ \mathbf{u}_{R1})$ and $\rho(\mathbf{u}_{T2},\ \mathbf{u}_{R2})$. The different target models are three 2-dimensional cases: Gaussian, Uniform Square, and Uniform Circle; and three 3-dimensional cases:

Gaussian, Uniform Cube, and Uniform Sphere. In all these cases, the correlation function becomes as follows

$$r = E[\rho(\mathbf{u}_{T1}, \mathbf{u}_{R1})\rho^*(\mathbf{u}_{T2}, \mathbf{u}_{R2})] \tag{2.6}$$

which turns into

$$r = E[e^{j\frac{2\pi}{\lambda}(\mathbf{u}_{T1}+\mathbf{u}_{R1})^T\mathbf{x}} e^{-j\frac{2\pi}{\lambda}(\mathbf{u}_{T2}+\mathbf{u}_{R2})^T\mathbf{x}}] \tag{2.7}$$

where, the expectation is taken *w.r.t.* the distribution on the random scatterer location $\mathbf{x}$. The dependence on the four direction vectors is through the one unit vector $\mathbf{u}$.

$$\mathbf{u} = \mathbf{u}_{T1} + \mathbf{u}_{R1} - \mathbf{u}_{T2} - \mathbf{u}_{R2} \tag{2.8}$$

In four of our six models, the dependence will only be through the scalar $A = |\mathbf{u}|$. Note that $A \leq 4$ by the triangle inequality.
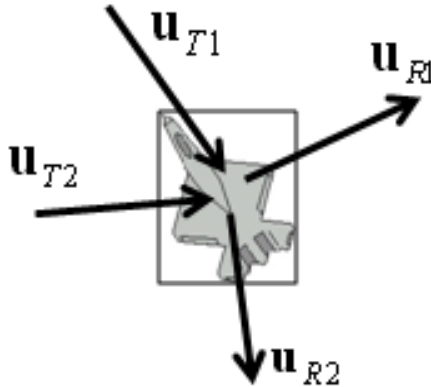
Figure 2.3: Unit Vectors Representation

The correlation therefore becomes as follows

$$r(\mathbf{u}) = \int e^{j\frac{2\pi}{\lambda}\mathbf{u}^T\mathbf{x}} f_{\mathbf{x}}(\mathbf{x}) \, d\mathbf{x} \tag{2.9}$$

where the integration is taken over 2-space or 3-space as appropriate according to the target models. In remainder of this section, we will evaluate equation 2.9 for different assumed density functions $f_{\mathbf{x}}(\mathbf{x})$. Appendix A illustrates the reflectivity correlation plots for all six target models. We now look into the six target models.

2.2.1 Model 1: 2D Gaussian

For $\mathbf{x} \in \mathbb{R}^2$, the density function for a Gaussian distribution is given by,

$$f_{\mathbf{x}}(\mathbf{x}) = \frac{1}{\sqrt{2\pi\sigma_x^2}} e^{-\frac{|\mathbf{x}|^2}{2\sigma_x^2}} \tag{2.10}$$

where, σ_x is the standard deviation of the scatterer location in each dimension (15). By circular symmetry of $f_{\mathbf{x}}(\mathbf{x})$ the correlation will be invariant to the direction of $\mathbf{u}$, and hence without loss of generality we can take $\mathbf{u} = A[1\ 0]^{\mathrm{T}}$. We obtain the following expression for the correlation function,

$$r(\mathbf{u}) = e^{-\frac{2\pi^2 A^2 \sigma_x^2}{\lambda^2}} \tag{2.11}$$

Note that $r(\mathbf{u}) = 1$, when either $\sigma_x^2 = 0$, which puts $\mathbf{x}$ at the origin with probability 1, or when $A = 0$. Figure 2.6 illustrates 2-D Gaussian model using the MATLAB GUI tool of varying size. The top image has 40 scatterers, and the center and bottom images have 20 and 5 scatterers respectively.

2.2.2 Model 2: Uniform Square

In this model the scatterer location is uniformly distributed on a square of the size $B\times B$. The square is oriented along the coordinate axes, which apparently destroys the circular symmetry, as we have noticed for the previous model. We define $\mathbf{u} = [u_x\ u_y]^{\mathrm{T}}$ and furthermore, $A_x = |u_x|$ and $A_y = |u_y|$. We have the correlation function as

$$r(\mathbf{u}) = \mathrm{sinc}\left(\frac{A_x B}{\lambda}\right) \mathrm{sinc}\left(\frac{A_y B}{\lambda}\right) \tag{2.12}$$

We use the definition of the *sinc* function

$$\mathrm{sinc}(x) = \frac{\sin(\pi x)}{\pi x} \tag{2.13}$$

Note that the argument of both the *sinc* functions contains the unit-less factor B/λ which is the length of one side of the square, in wavelengths. Note also that the correlation is 1 when either $A_x = A_y = 0$, or $B = 0$. Figure 2.7 illustrates this model of varying size. Similar to 2-D Gaussian demonstration, the images have 40, 20, and 10 scatterers.

2.2.3 Model 3: Uniform Circle

Here $\mathbf{x}$ is uniformly distributed on a unit circle or radius R, denoted by $C(R)$. For the correlation function, we have

$$r(\mathbf{u}) = \frac{1}{\pi R^2} \iint_{C(R)} e^{j\frac{2\pi \mathbf{u}^T \mathbf{x}}{\lambda}} \, d\mathbf{x} \tag{2.14}$$

By the circular symmetry of $f_{\mathbf{x}}(\mathbf{x})$ we can take $\mathbf{u} = A[1\ 0]^T$ and thus the integral becomes

$$r(\mathbf{u}) = \iint_{C(R)} e^{j\frac{2\pi A x}{\lambda}} \, dx dy \tag{2.15}$$

Transforming into polar coordinates, and after performing integration and appropriate algebra, the correlation function becomes

$$r(\mathbf{u}) = \frac{2J_1\left(\frac{2\pi A R}{\lambda}\right)}{\left(\frac{2\pi A R}{\lambda}\right)} \tag{2.16}$$

The function $2J_1(u)/u$ is the *jinc* function (20,21). It appears qualitatively similar to *sinc* function: it is symmetric, has a maximum value of 1 at $u = 0$. Our final expression for correlation thus becomes

$$r(\mathbf{u}) = jinc\left(\frac{2\pi A R}{\lambda}\right) \tag{2.17}$$

Note that the argument depends on R/λ, referred as the target extent of the model, which is the radius of the circle in terms of wavelengths. Figure 2.8 illustrates this model for three different target extents.

2.2.4 Model 4: 3D Gaussian

This is an expansion into three dimensions from 2-D Gaussian model. Here, $\mathbf{x}$ forms a spherical Gaussian distribution (15) with density function

$$f_{\mathbf{x}}(\mathbf{x}) = (2\pi \sigma_x^2)^{-3/2} \, e^{-\frac{|\mathbf{x}|^2}{2\sigma_x^2}} \tag{2.18}$$

As in the 2D Gaussian example, we can take $\mathbf{u} = A[1\ 0\ 0]^{\mathrm{T}}$, and thus the triple integral in the expectation reduces to a single integral. We assume circular symmetry, and hence obtain the correlation function to be

$$r(\mathbf{u}) = e^{-\frac{2\pi^2 A^2 \sigma_x^2}{\lambda^2}} \tag{2.19}$$

Figure 2.9 illustrates 3D Gaussian model of varying target extent.

2.2.5 Model 5: Uniform Cube

This is basically a straightforward extension of the 2D uniform square case. Here, $\mathbf{x}$ is uniformly distributed over a cube of length B on a side. Since the cube is aligned along the coordinate axes, we cannot assume spherical symmetry. We set $\mathbf{u} = [u_x\ u_y\ u_z]^{\mathrm{T}}$ and obtain the following for the correlation function

$$r(\mathbf{u}) = \mathrm{sinc}\left(\frac{A_x B}{\lambda}\right) \mathrm{sinc}\left(\frac{A_y B}{\lambda}\right) \mathrm{sinc}\left(\frac{A_z B}{\lambda}\right) \tag{2.20}$$

Similar to the 2D model, the correlation will be 1 when either $A_x = A_y = A_z = 0$, or $B = 0$. Figure 2.10 depicts this model for different target extent.

2.2.6 Model 6: Uniform Sphere

For this model, $\mathbf{x}$ is uniformly distributed on a sphere of radius R, denoted by $S(R)$. The desired expression for the correlation function is

$$r(\mathbf{u}) = \frac{3}{4\pi R^3} \iiint_{S(R)} e^{j\frac{2\pi \mathbf{u}^{\mathrm{T}} \mathbf{x}}{\lambda}} d\mathbf{x} \tag{2.21}$$

Because of spherical symmetry, we can, without loss of generality, take $\mathbf{u} = A[0\ 0\ 1]^{\mathrm{T}}$, along the z-axis, and therefore we get

$$r(\mathbf{u}) = \frac{3}{4\pi R^3} \int_0^R \int_0^\pi e^{j\frac{2\pi A r \cos\theta}{\lambda}} \sin\theta d\theta\, r^2 dr \tag{2.22}$$

For mathematical convenience, we introduce the parameter $\alpha = (2\pi A)/\lambda$. With some necessary substitutions and algebra, we obtain

$$r(\mathbf{u}) = \frac{3(\sin(\alpha R) - (\alpha R)\cos(\alpha R))}{(\alpha R)^3} \tag{2.23}$$

In the above expression (2.23) we notice the function

$$f(u) = \frac{3(\sin(u) - u\cos(u))}{u^3} = \frac{3j_1(u)}{u} \tag{2.24}$$

where $j_l(u)$ is the spherical Bessel function of the first kind (22). The function $f(u)$ is similar to a *sinc* function, shown in equation 2.13, symmetric with maximum occurring at $f(0) = 1$. Hence, the correlation functions can be written as

$$r(\mathbf{u}) = \frac{3j_1\left(\frac{2\pi AR}{\lambda}\right)}{2\pi A\left(\frac{R}{\lambda}\right)} \tag{2.25}$$

2.3 Monostatic and Bistatic Cases

Apart from depicting the 6 models by means of MATLAB GUI-based simulation tools, each target's reflectivity is also shown for two cases – monostatic and bistatic. Several scatterers are generated on the target for reflectivity. The number of scatterers is selected by the user, so more the number of scatterers the better the reflectivity. Once each target has a set location, it is given a random complex reflectivity. This reflectivity is used to determine the overall target reflectivity for various view angles for both the monostatic and bistatic cases.

Monostatic case shows the variation in the magnitude of complex reflectivity as a function of the view angle for collocated transmitter and receiver. The location of the receiver and transmitter is determined by the *View Distance Radius*, which inputs the distance from the origin of the target that the transmitter and receiver are located. An array of transmitter and receiver coordinates is created making a circle around the center of the target at the inputted distance. The transmitter and receiver are always located on the x-y plane and therefore the z-values in the transmitter and receiver coordinates are zero. Determining the complex reflectivity for the target is the same for the 2-D and 3-D target models, which has been described below.

To determine the complex reflectivity the distance from the transmitter and the receiver to center of the target is calculated, along with the distance from the transmitter and receiver to each separate point of the target. The difference between these distances is then calculated and the value is divided by the speed of light, c. This uses the fact that the transmitted wave is traveling at the speed of light, and the difference in distance creates a difference in time for the signal to be received from each point in the target. These differences in time cause a change in phase, which is given by

$$\varphi_i = 2\pi f_c \tau_i \tag{2.26}$$

where, τ_i is the calculated differences in time, and f_c is the center frequency of the system. The figure below (Figure 2.4) depicts the monostatic radar system setup.
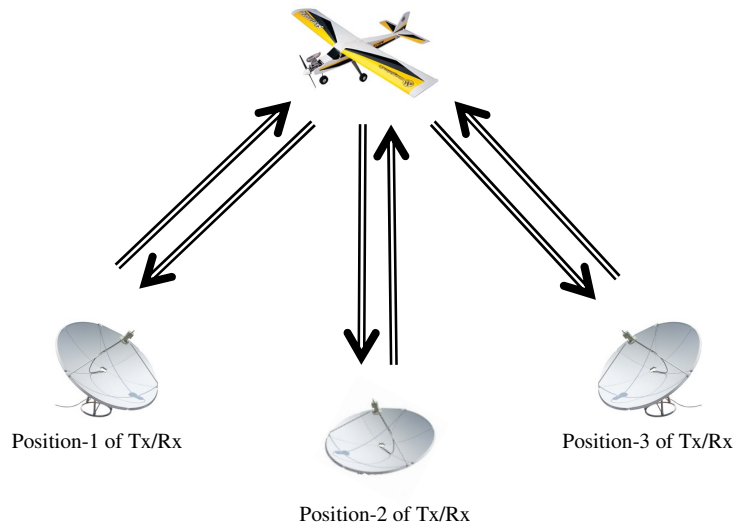

Figure 2.4: Monostatic Case for Radar Systems

Each point's complex reflectivity phase term is then determined from the expression

$$R_i = \rho_i e^{-j2\pi\varphi_i} \tag{2.27}$$

where ρ_i is the random complex reflectivity of the given point in the target. These values are then summed up for all of the points in the target. The absolute value is then taken and the values are converted to dB. They are then plotted for 360° around the target.
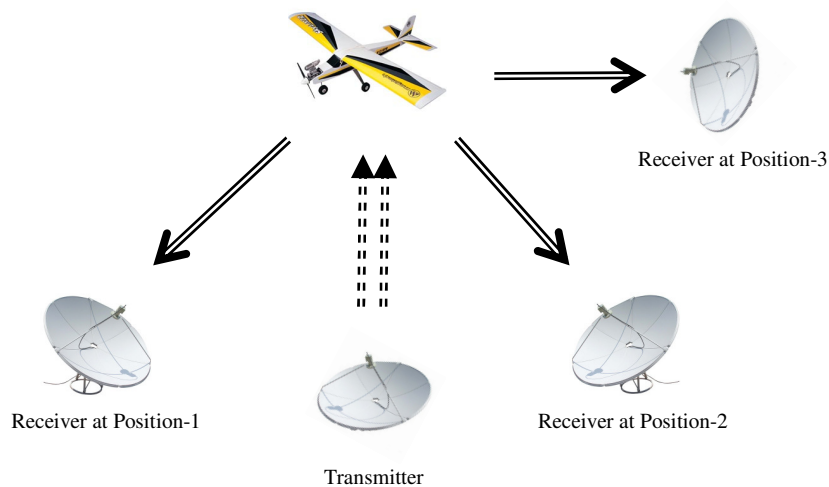
Figure 2.5: Bistatic Case for Radar Systems

The same analysis is done for the bistatic case, which shows the variation in the magnitude of the complex reflectivity as a function of the receiver view angle, with the difference being the location of the transmitter and the receiver. Here the transmitter is always located at the inputted distance away from the center of the target on the x-axis. The receiver location is then an array of coordinates creating a circle of inputted radius around the target center. The bistatic case changes overall distances that the transmitted signals have to travel and ultimately causes a different complex reflectivity. Figure 2.5 shows the bistatic radar setup.

2.4 Target Model Illustration

The following sequence of figures show the six models, described previously, by MATLAB simulation and GUI. These have been designed by John Vander Laan. The first/top GUI image in each figure displays target in bigger size with more scatterers. And in the following two GUI image, target is smaller in size with lesser scattering points. Both the number of scatterers and size of the target are user inputs so that they can be varied accordingly to get an idea of how the monostatic and bistatic alters with target extent and number of scatterers present.
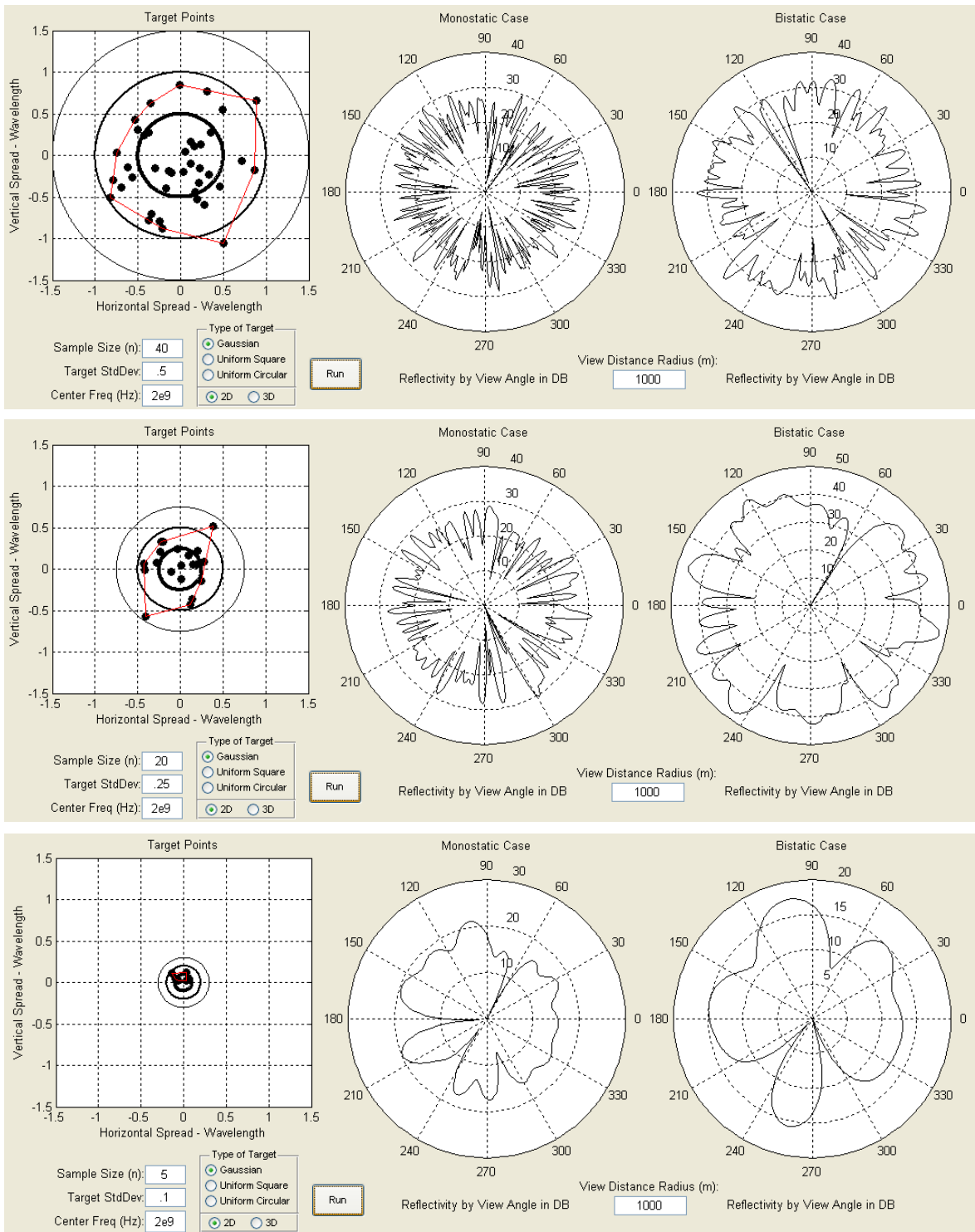
Figure 2.6: 2-D Gaussian

(Top) Scatterers: 40, Size: 0.5λ   (Center) Scatterers: 20, Size: 0.25λ   (Bottom) Scatterers: 5, Size: 0.1λ
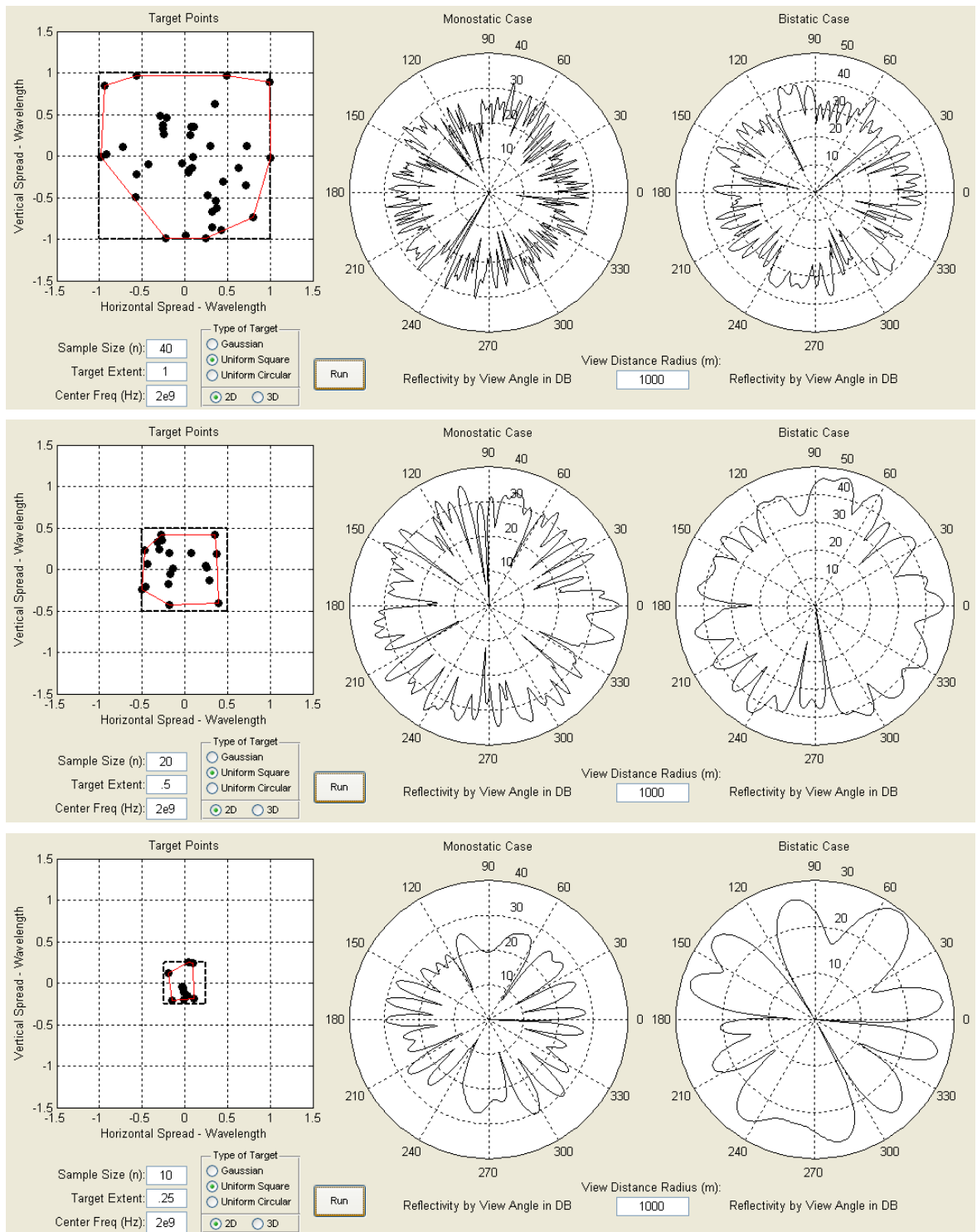
Figure 2.7: 2-D Uniform Square

(Top) Scatterers: 40, Size: 1λ   (Center) Scatterers: 20, Size: 0.5λ   (Bottom) Scatterers: 10, Size: 0.25λ
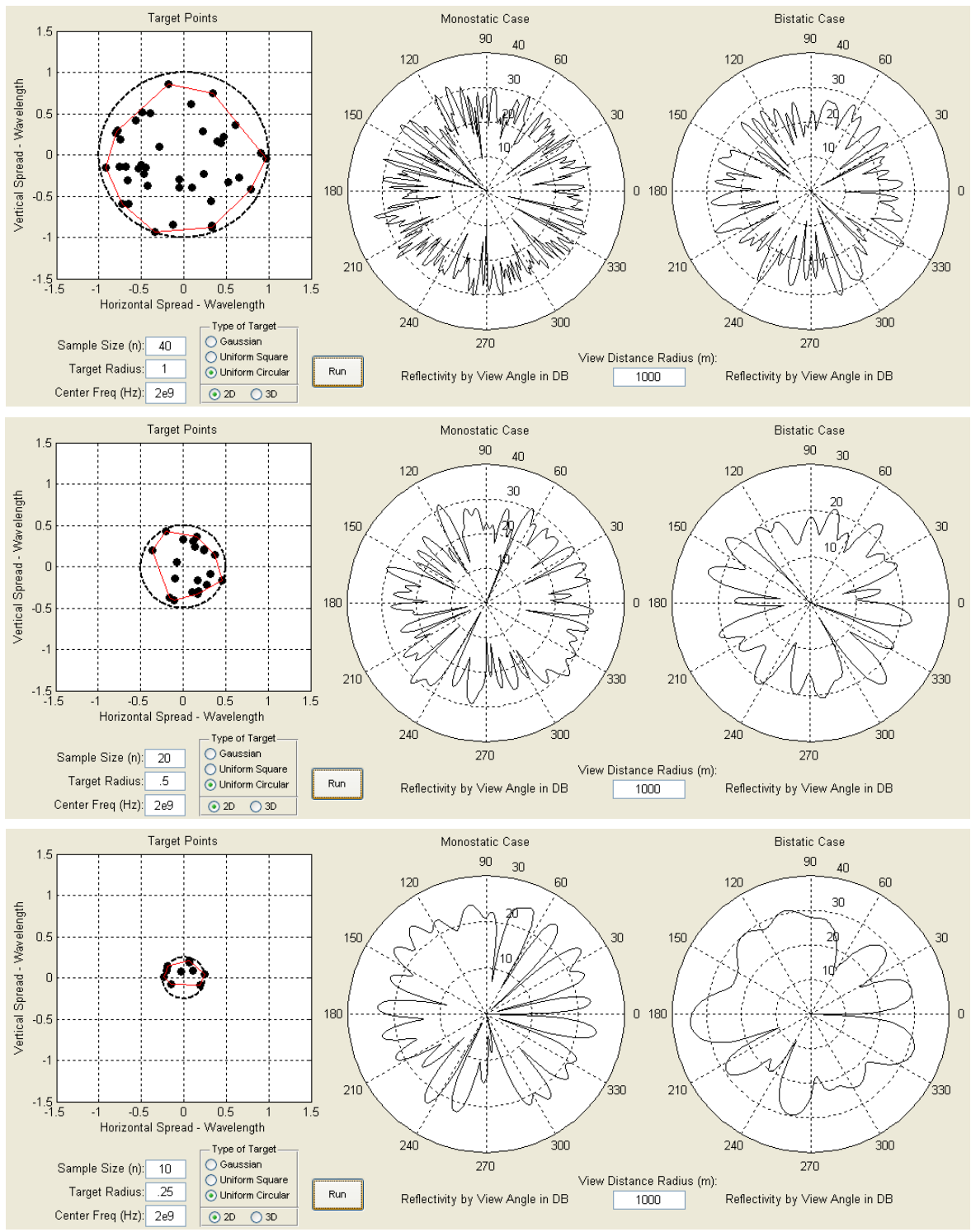
Figure 2.8: 2-D Uniform Circle

(Top) Scatterers: 40, Size: 1λ   (Center) Scatterers: 20, Size: 0.5λ   (Bottom) Scatterers: 10, Size: 0.25λ
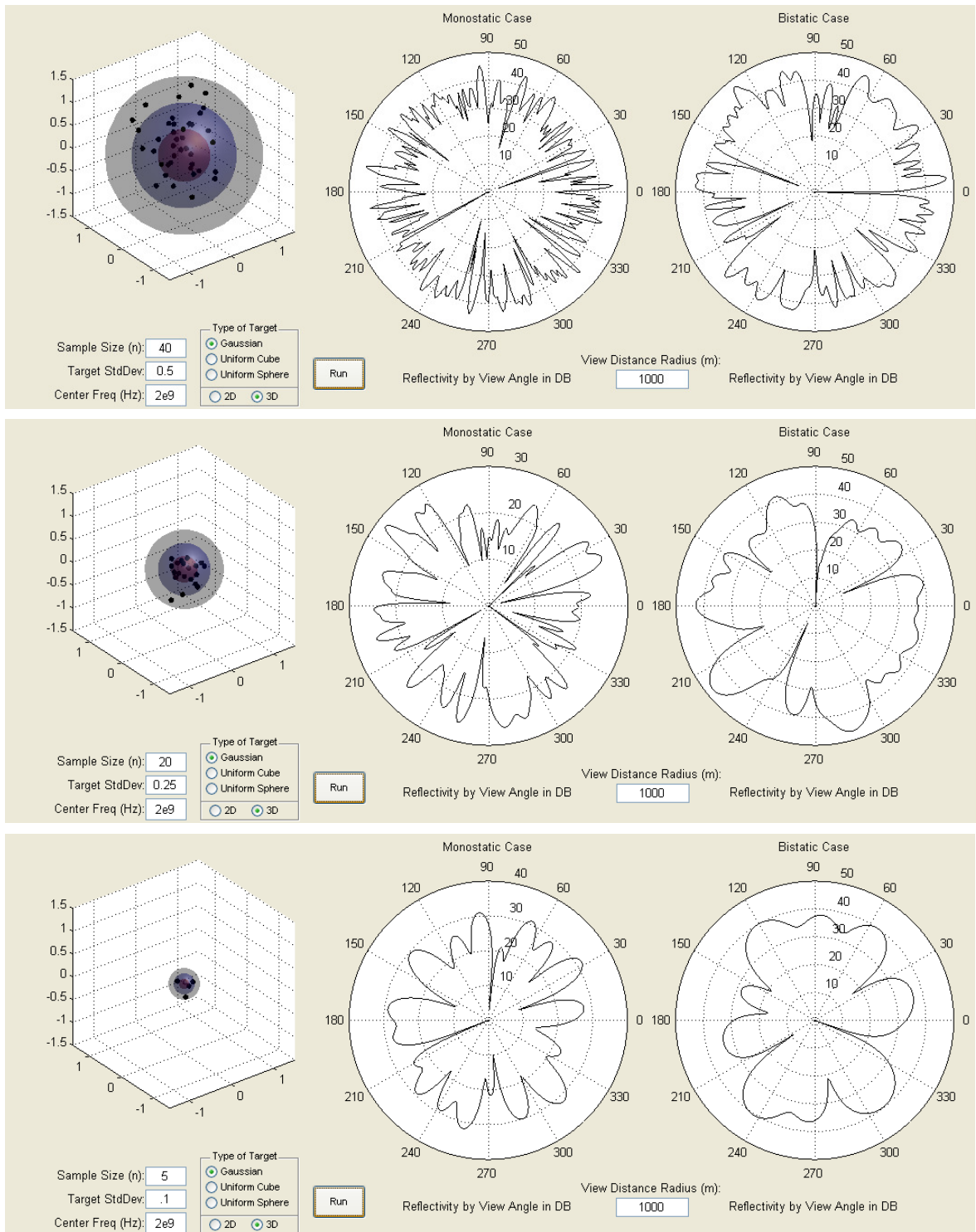
Figure 2.9: 3-D Gaussian

(Top) Scatterers: 40, Size: 0.5λ   (Center) Scatterers: 20, Size: 0.25λ   (Bottom) Scatterers: 5, Size: 0.1λ
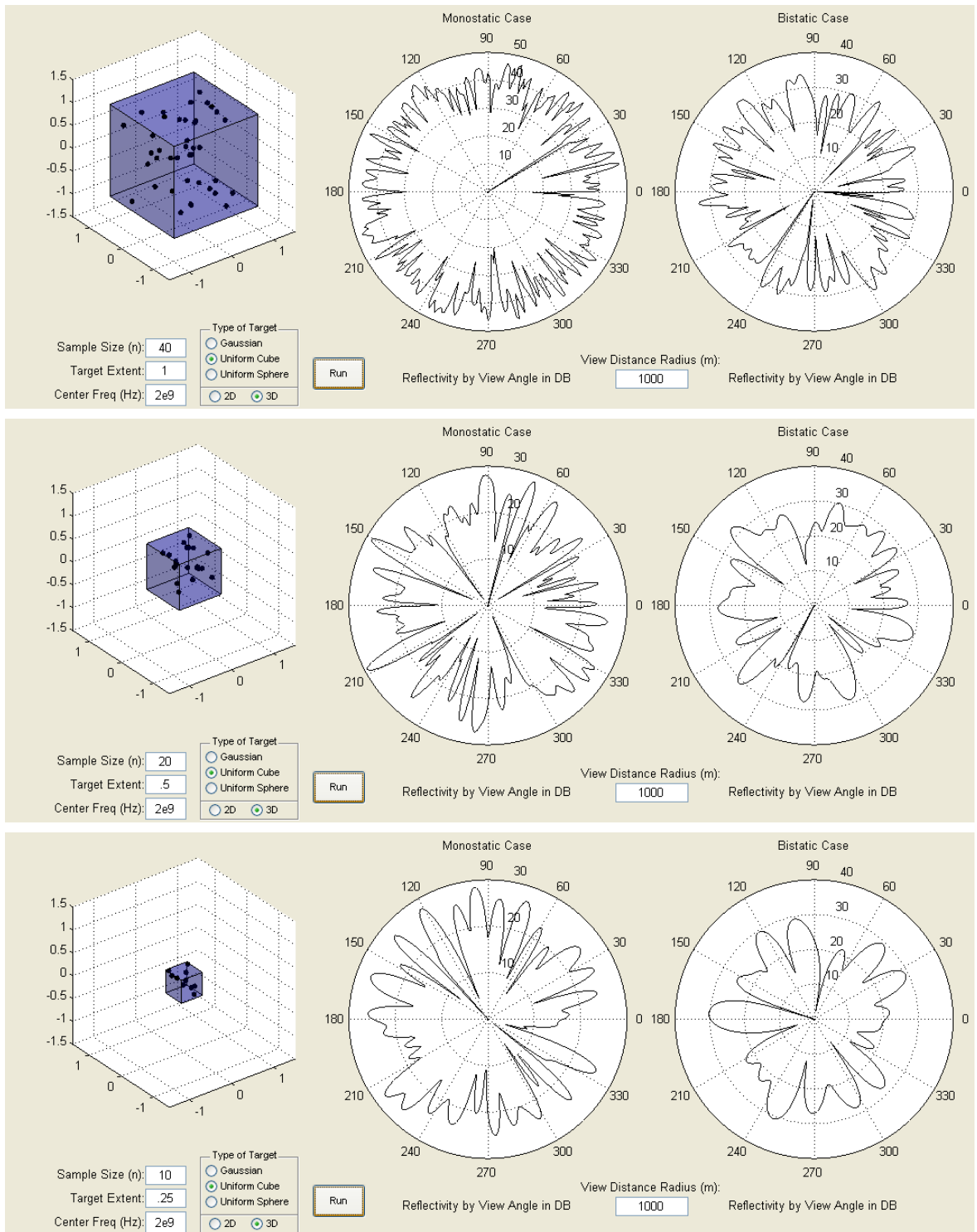
Figure 2.10: 3-D Uniform Cube

(Top) Scatterers: 40, Size: 1λ   (Center) Scatterers: 20, Size: 0.5λ   (Bottom) Scatterers: 10, Size: 0.25λ
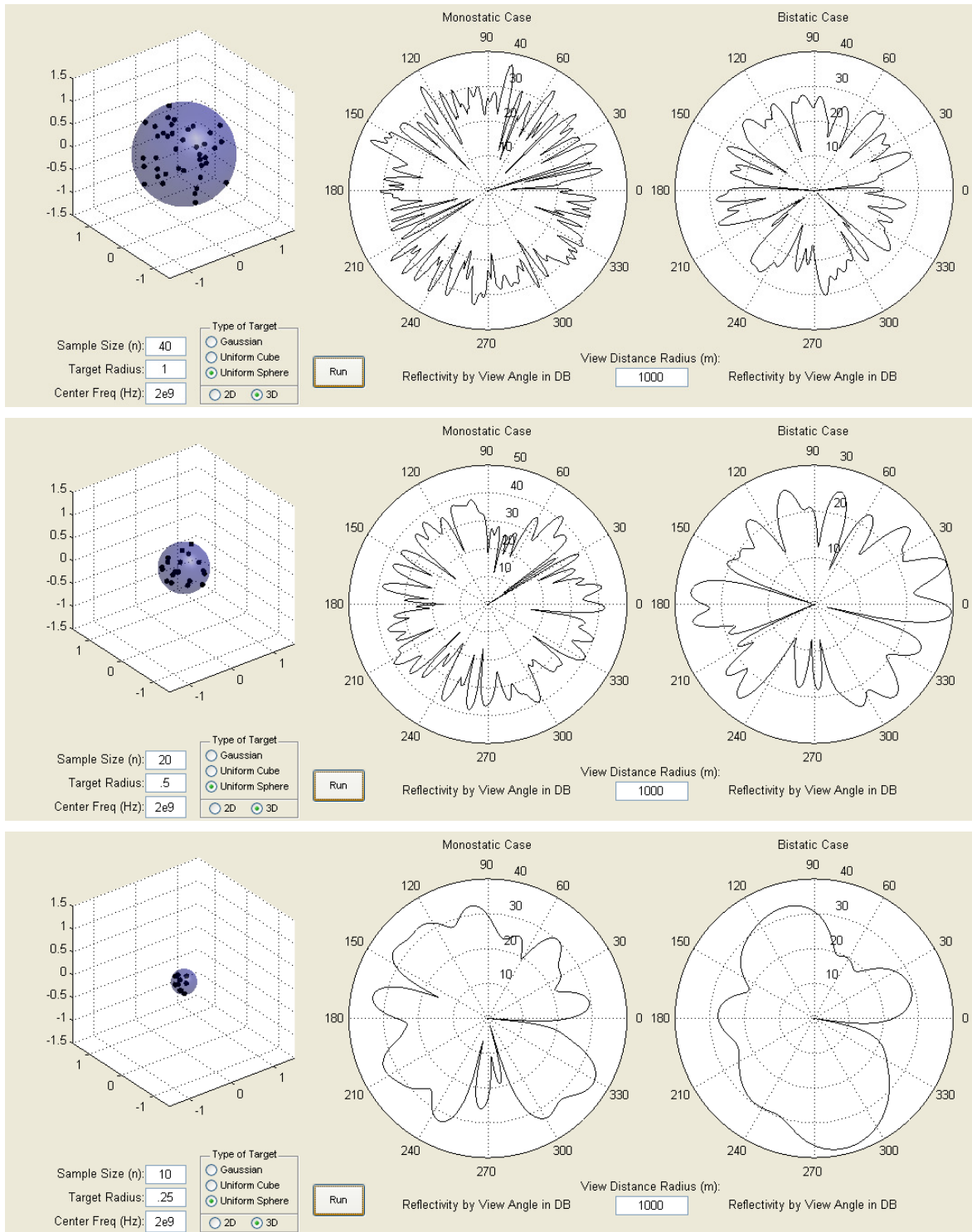
Figure 2.11 : 3-D Uniform Sphere

(Top) Scatterers: 40, Size: 1λ   (Center) Scatterers: 20, Size: 0.5λ   (Bottom) Scatterers: 10, Size: 0.25λ

Chapter 3 ~ Detection Problem

3.1 Overview

In our MIMO radar system, we have M_T spatially distributed transmitters and M_R spatially distributed receivers. A key assumption being made here is that all T/R modules are cooperating and that all the receivers can respond to all the transmitted signals. To keep matters simple, we note that the transmitters and receivers are not collocated, as this will eliminate any possibility of having reciprocal paths for which bistatic reflectivities are equal. Here we have $M_T M_R$ distinct bistatic paths, for which we can compute target reflectivity using the models. For our detector model we are using four transmitters, and four receivers ($M_T = 4$, $M_R = 4$). In a standard grid model, the transmitters and receivers are located at the following coordinates in 2-dimensional setup

$$Tx_1 = (-4,5) \quad Tx_2 = (-3,5) \quad Tx_3 = (-2,5) \quad Tx_4 = (-1,5)$$
$$Rx_1 = (1,5) \quad Rx_2 = (2,5) \quad Rx_3 = (3,5) \quad Rx_4 = (4,5)$$

(3.1)

and in 3-dimensional setup

$$Tx_1 = (-4,5,-1) \quad Rx_1 = (1,5,-1)$$
$$Tx_2 = (-3,5,-1) \quad Rx_2 = (2,5,-1)$$
$$Tx_3 = (-2,5,-1) \quad Rx_3 = (3,5,-1)$$
$$Tx_4 = (-1,5,-1) \quad Rx_4 = (4,5,-1)$$

(3.2)

We take the target to be at the center of the grid (0, 0) or (0, 0, 0). Figure 3.1 illustrates this bistatic radar system setup for our detector model.

3.2 Devising the Detection Problem

Once we have established the setup in Figure 3.1, we proceed to compute $\mathbf{u}_T$ and $\mathbf{u}_R$, the unit vectors pointing towards the transmitters and receivers respectively, using the equation 2.8, followed by the scalar $A = |\mathbf{u}|$, where the size of A is 16×16. The diagonal terms of A are all zero. Using A, we calculate the complex reflectivity for our system for each of the six models using the correlation equations.
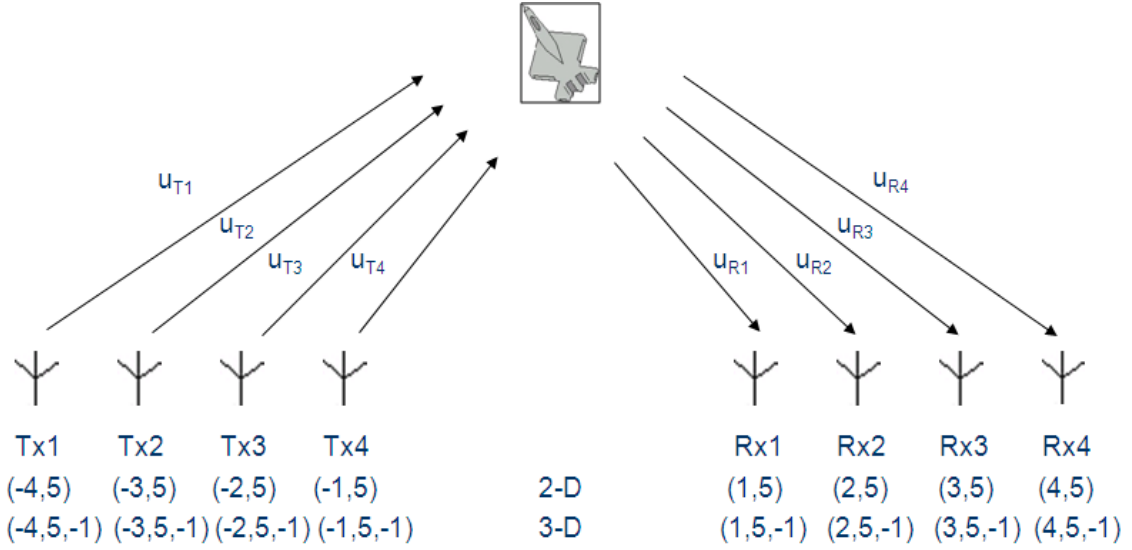
Figure 3.1: MIMO System Setup for Target Detection

It is worth mentioning that the signals transmitted by these transmitters are coded waveforms that can be represented by a discrete sequence of complex code values. There are $M_T = 4$ such signals of length N, where N is the time-bandwidth product for a single pulse approximately. The transmitted signal can be represented as an $N \times M_T$ matrix $\mathbf{S}$ (for our setup, we have $N = 1000$). We have used orthogonal signal $\mathbf{S}$ for this MIMO system that will be discussed further in the following section.

The complex reflectivity $\rho(i, j)$ is the reflectivity for the bistatic path from the transmitter i to the receiver j, and these can all be represented by a channel matrix $\mathbf{H}$ that is $M_T \times M_R$ in size. The steps we take to obtain $\mathbf{H}$ are given as follows,

- Find complex reflectivity, R_{cov} using correlation equations
- Cholesky Decomposition of R_{cov} to obtain an upper-triangular matrix
- Multiply the upper-triangular matrix by $CN(0, \mathbf{I})$ of size 1×16
- Reshape the above 1×16 matrix to yield the 4×4 channel matrix $\mathbf{H}$

Assuming the signals are time-aligned on the target (a non-trivial assumption made for simplicity of the detection problem) the $N \times M_R$ matrix of received signals can be written as shown by the expression (3.3), where $\mathbf{W}$ represents additive white noise. Note that R_{cov} must be a positive definite matrix.

$$\mathbf{Z} = \mathbf{SH} + \mathbf{W} \qquad (3.3)$$

We perform QR decomposition on the signal matrix **S** to result in an orthogonal matrix **Q** and an upper triangular matrix **R** of economy size. Without any loss of information, we perform the following operation on equation (3.3)

$$\mathbf{Y} = \mathbf{Q}^H \mathbf{Z} = \mathbf{Q}^H \mathbf{SH} + \mathbf{Q}^H \mathbf{W} \qquad (3.4)$$

The resulting $M_T M_R$ values in **Y** are then stacked into a $K \times 1$ column vector $\mathbf{y}$, which is then used to devise the two hypotheses for target detection.

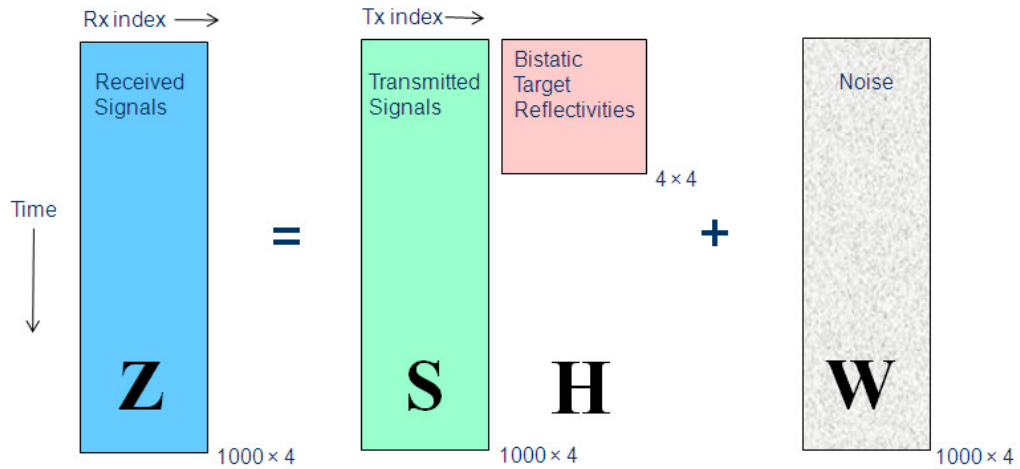$$\mathbf{y} = \mathbf{x} + \mathbf{n} \qquad (3.5)$$

Figure 3.2: Matrix Dimension representation of (3.3)

3.3 Transmitted Signal

We have used statistically independent signals, or *orthogonal signals*, which are stacked in a long-and-skinny vector denoted by **S** (see Figure 3.2) of size $N \times M_R$. This allows us to assume that all the transmit signals are noncoherent waveforms. The steps shown below were followed to generate the orthogonal signals,

- The $N \times M_R$ complex exponential matrix in, Figure 3.3, is generated
- Spreading signal: $N \times 1$ column vector of form $- e^{j\varphi}$, where $\varphi \sim \mathrm{U}[0, 2\pi]$ i.i.d.
- Columns of the complex exponential matrix is element-wise multiplied by the spreading signal, which spreads the spectrum of each column

$$
\begin{pmatrix}
1 & 1 & 1 & 1 \\[2mm]
e^{\frac{j2\pi(1)(1)}{N}} & e^{\frac{j2\pi(1)(2)}{N}} & e^{\frac{j2\pi(1)(3)}{N}} & e^{\frac{j2\pi(1)(4)}{N}} \\[2mm]
e^{\frac{j2\pi(2)(1)}{N}} & \cdots & \cdots & e^{\frac{j2\pi(2)(4)}{N}} \\[2mm]
\vdots & \ddots & & \vdots \\[2mm]
\vdots & & \ddots & \vdots \\[2mm]
e^{\frac{j2\pi(k-1)(1)}{N}} & \cdots & \cdots & e^{\frac{j2\pi(k-1)(4)}{N}}
\end{pmatrix}
$$

Figure 3.3: Complex Exponential Matrix of **S**

3.4 Hypothesis Testing

After orthogonal **S** is generated and undergone QR decomposition (16), we look into the hypothesis testing problem, which is

$$H0: \quad \boldsymbol{y} \sim CN(0, \sigma^2 \mathbf{I}) \tag{3.6}$$

$$H1: \quad \boldsymbol{y} \sim CN(0, \alpha \mathbf{R}_x + \sigma^2 \mathbf{I}) \tag{3.7}$$

This is the familiar Gauss-Gauss detection problem (5,10). For the finite dimensional complex Gaussian version, this testing problem can be simplified as follows,

- The observation is first scaled so that variance of each noise component is 1
- A rotation is then applied to observation to which noise covariance is invariant
- This operation transforms the signal covariance into a diagonal matrix Λ
- Eigenvalue decomposition is performed on $\mathbf{R}_x$ as the next step
- The diagonal elements λ_k are the eigenvalues of $\mathbf{R}_x$
- Scalar component, α in (3.6) is known and is responsible for SNR

The transformed observation is denoted in vector form **v**, having the following hypothesis

$$H0: \quad \mathbf{v} \sim CN(0, \mathbf{I}) \tag{3.8}$$

$$H1: \quad \mathbf{v} \sim CN(0, \alpha \Lambda + \mathbf{I}) \tag{3.9}$$

3.4.1 Gauss-Gauss Detection Problem

In (3.6) we come across $\mathbf{R}_x$ which is obtained by the following expression. As a quick refresher, R_{cov} is the complex reflectivity matrix computed for each model from the correlation functions derived in Chapter 2.

$$\mathbf{R}_x = A_{diag} * R_{cov} * A_{diag}^T \tag{3.10}$$

However, A_{diag} is a $M_T M_R \times M_T M_R$ diagonal matrix acquired by stacking the elements of matrix $\mathbf{R}$ (from economy size QR decomposition of $\mathbf{S}$) across its diagonal. Figure 3.4 gives a visual representation of this matrix.

$$\mathbf{A}_{diag} = \begin{pmatrix} \mathbf{R}_{4\times4} & \mathbf{0} & \mathbf{0} & \mathbf{0} \\ \mathbf{0} & \mathbf{R}_{4\times4} & \mathbf{0} & \mathbf{0} \\ \mathbf{0} & \mathbf{0} & \mathbf{R}_{4\times4} & \mathbf{0} \\ \mathbf{0} & \mathbf{0} & \mathbf{0} & \mathbf{R}_{4\times4} \end{pmatrix}_{16\times16}$$

Figure 3.4: $\mathbf{A}_{diag}$ matrix representation

After Eigenvalue decomposition of $\mathbf{R}_x$, hypothesis $H1$ is obtained by

$$H1 \sim \mathbf{u}_{mat}^T * y \tag{3.11}$$

where, $\mathbf{u}_{mat} \rightarrow$ eigenvectors following the Eigenvalue decomposition of $\mathbf{S}$

         $y \rightarrow$ computed from equation (3.5)

3.4.2 Eigenvalue Distribution

The eigenvalues, λ_k exhibit exponential properties for both 2-D and 3-D Gaussian models. However, for the other four models, the eigenvalues decay rapidly with one of the values dominating. The eigenvalue distribution stem plots for each model are shown in the following sections, for two different sizes. It is worth observing that the eigenvalue plots depict uniform distribution with the increasing target extent. This phenomenon is consistent with all six models suggesting that the received signals become uncorrelated at the receiver end when the target expands in size appreciably.
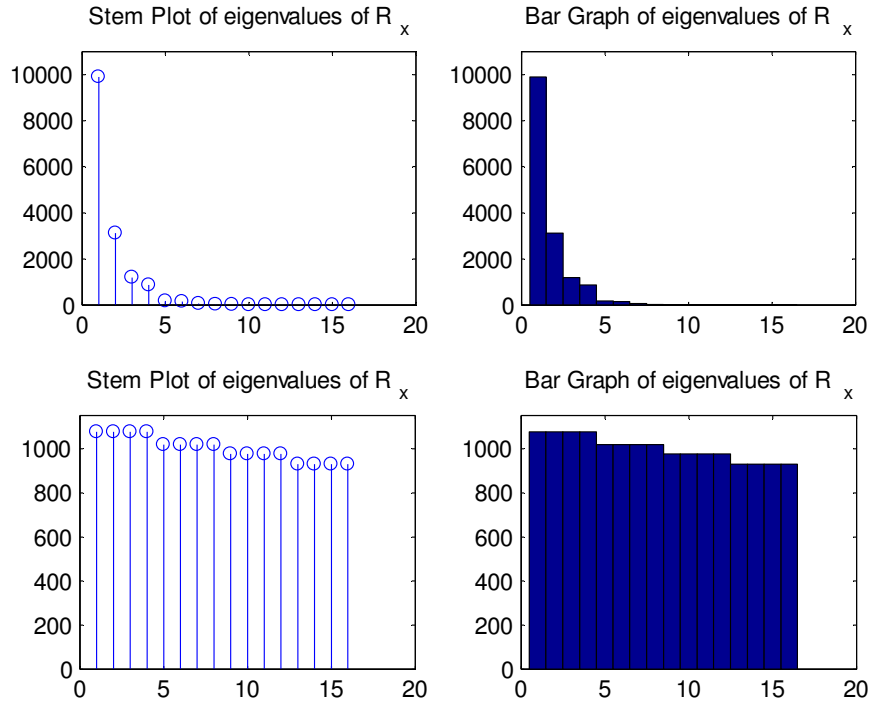
Figure 3.5: Eigenvalue Distribution for 2-D Gaussian

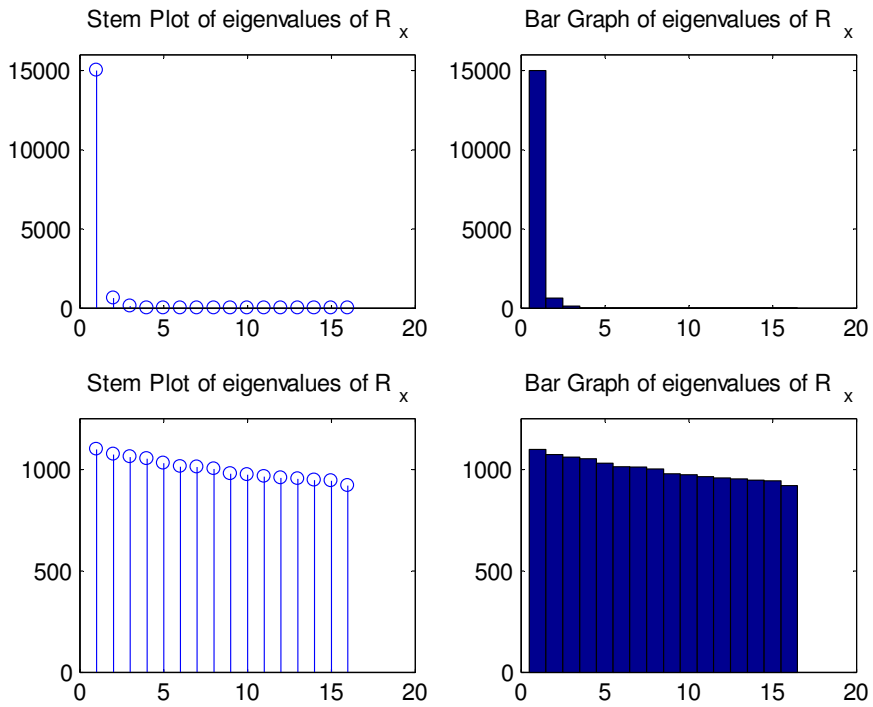Target Extent: (Top) 0.5λ and (Bottom) 50λ

Figure 3.6: Eigenvalue Distribution for 2-D Uniform Square

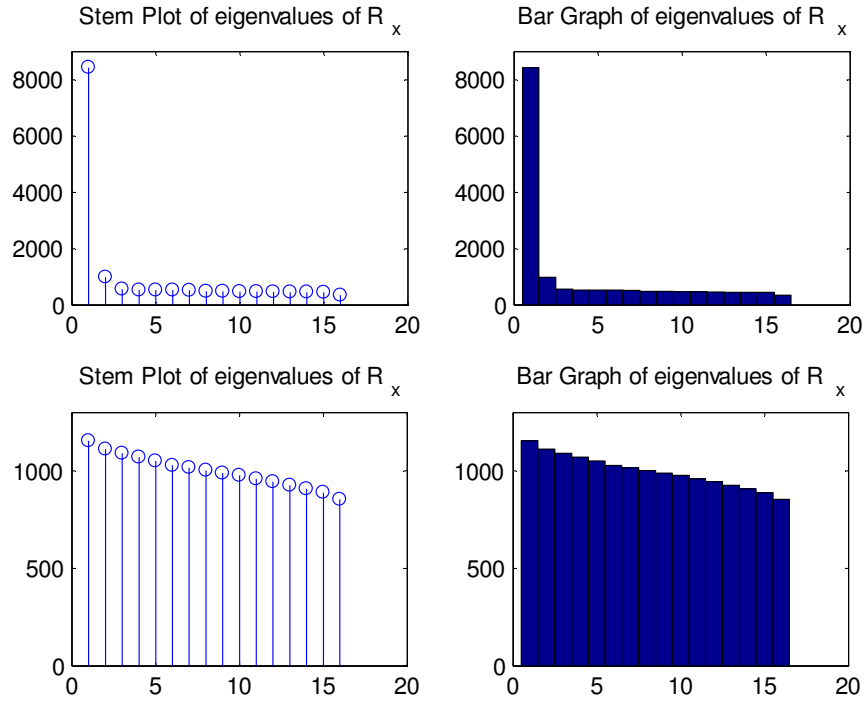Target Extent: (Top) 0.5λ and (Bottom) 50λ

Figure 3.7: Eigenvalue Distribution for 2-D Uniform Circle
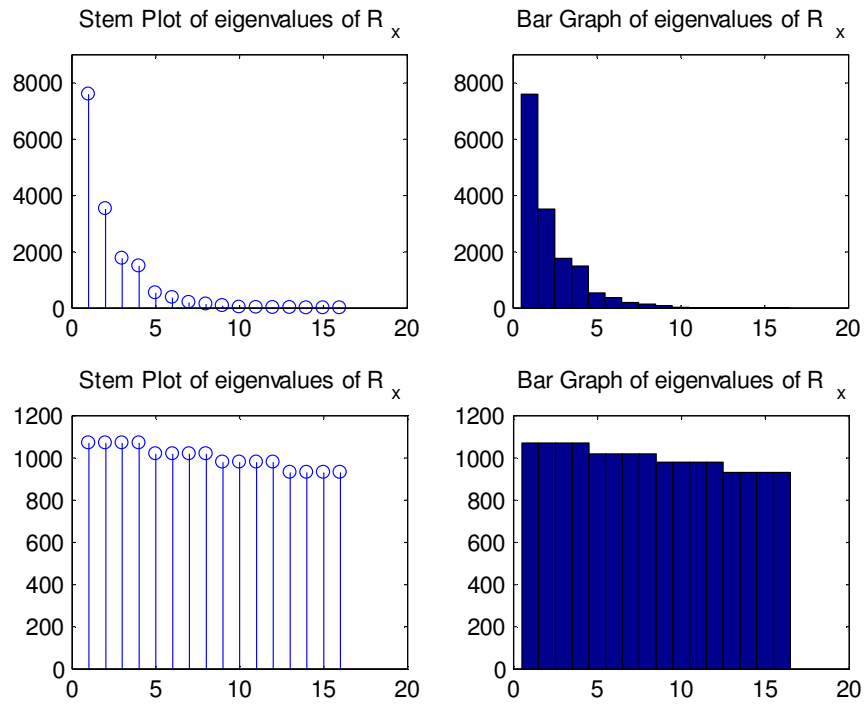
Target Extent: (Top) 0.5λ and (Bottom) 50λ

Figure 3.8: Eigenvalue Distribution for 3-D Gaussian

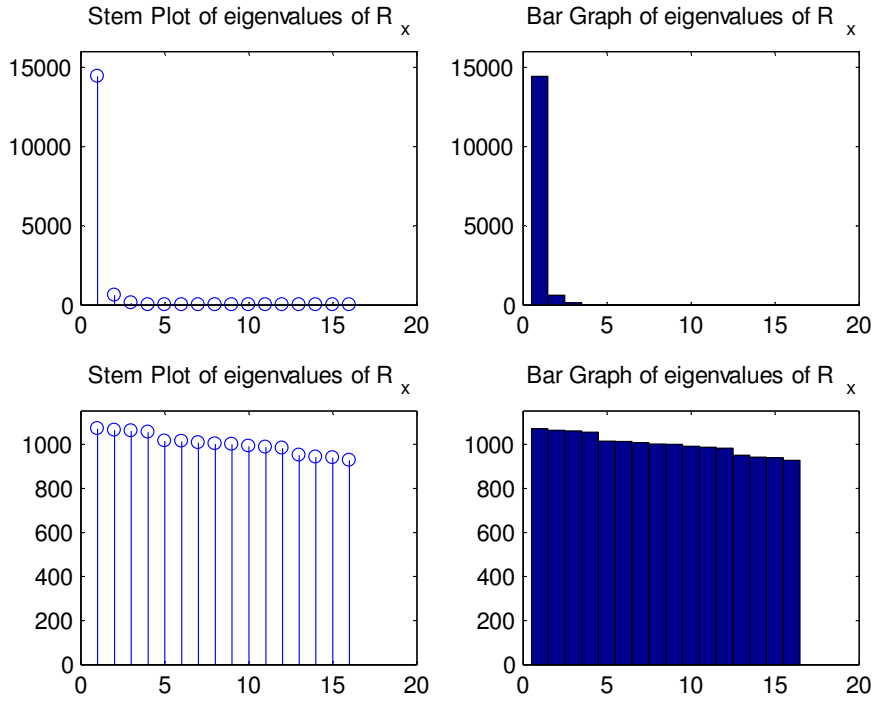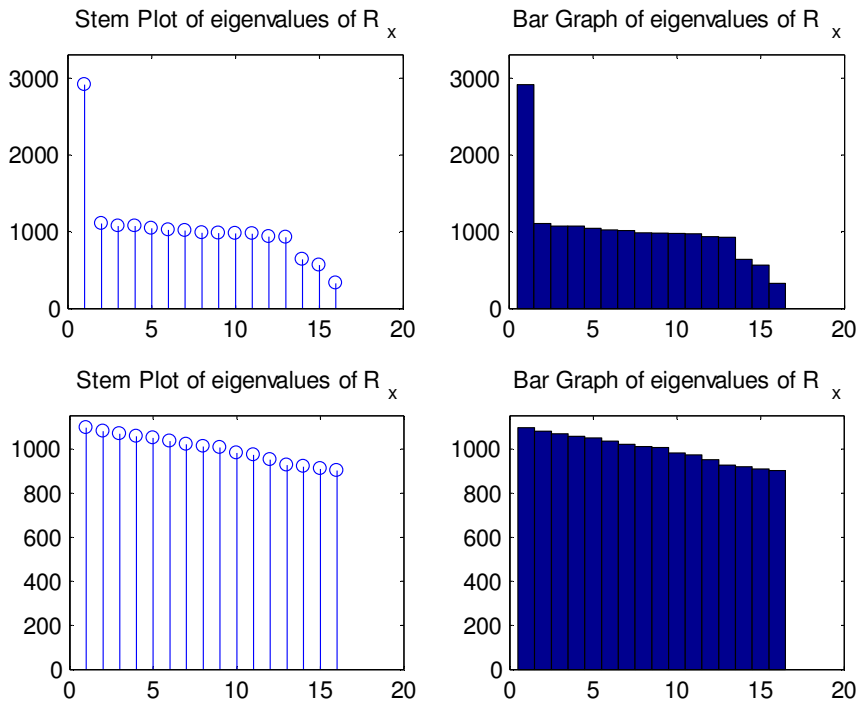Target Extent: (Top) 0.5λ and (Bottom) 50λ

Figure 3.9: Eigenvalue Distribution for 3-D Uniform Cube

Target Extent: (Top) 0.5λ and (Bottom) 50λ

Figure 3.10: Eigenvalue Distribution for 3-D Uniform Sphere

Target Extent: (Top) 0.5λ and (Bottom) 50λ

3.5 Test Statistics

At this point, we have generated our data for both $H0$ and $H1$ hypothesis. The likelihood ratio (17,18) becomes

$$L(\mathbf{x}) = \frac{p(\mathbf{x}; H1)}{p(\mathbf{x}; H0)} \tag{3.12}$$

$$L(\mathbf{x}) = \frac{\pi^{-K}\left(\prod_{k=1}^{K}(1 + \lambda_k)\right)^{-1}\left(\prod_{k=1}^{K} e^{-\frac{|v_k|^2}{1+\lambda_k}}\right)}{\pi^{-K}\left(\prod_{k=1}^{K} e^{-|v_k|^2}\right)} \tag{3.13}$$

After some algebraic manipulation, we obtain the following test statistic shown by the expression below. Plots of the test statistics for each target model are provided below (see Figures $3.11-3.16$).

The plots are histograms, with each plot having one thousand bars of equal bean width. For each simulation, the target extent is kept constant at 0.25λ, and there are 2×10^6 data points under each density function. The data points under each hypothesis, $H0$ and $H1$, are stored in different arrays and the test statistics were computed under each of the hypothesis. The two hypotheses histograms are first plotted separately, and then put together in one plot. Hence, the top plot in each figure depicts histogram of hypothesis $H0$, the center plot is the histogram of hypothesis $H1$, and the bottom plot is both the hypotheses combined on the same set of axes. Notice that for all the six different target models the histograms for both $H0$ and $H1$ do not vary appreciably, which is what we have expected while generating data for the detection problem.

$$\mathbf{t} = \sum_{k=1}^{K} |v_k|^2 \left(\frac{\lambda_k}{1 + \lambda_k}\right) \tag{3.14}$$

where, $K \rightarrow M_T * M_R = 16$

$v_k \rightarrow$ each element under $H0$ and $H1$
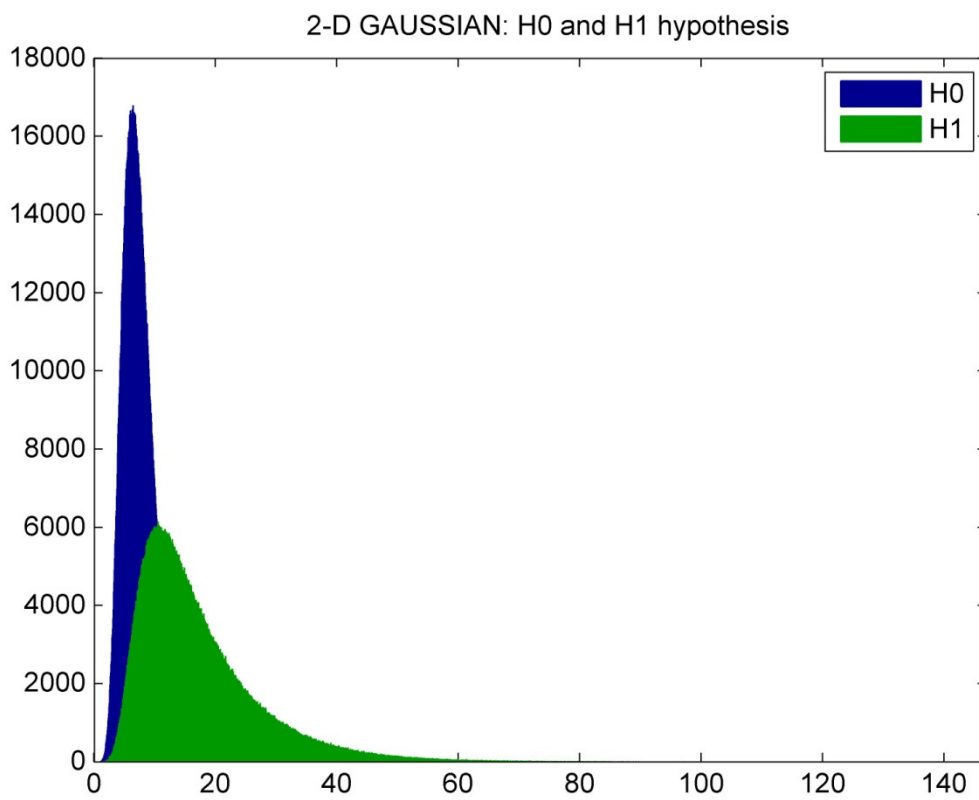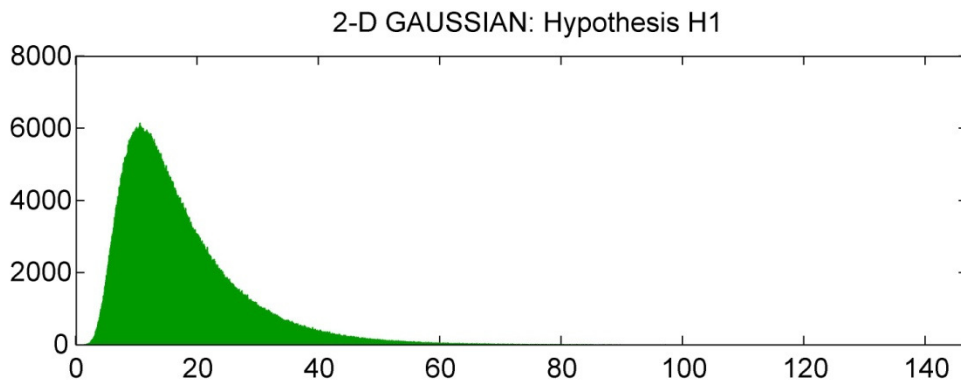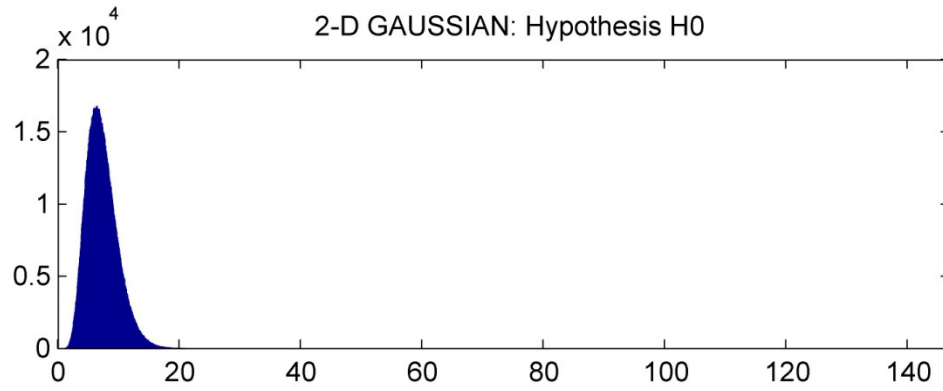
$\lambda_k \rightarrow$ eigenvalues or $\mathbf{R}_x$

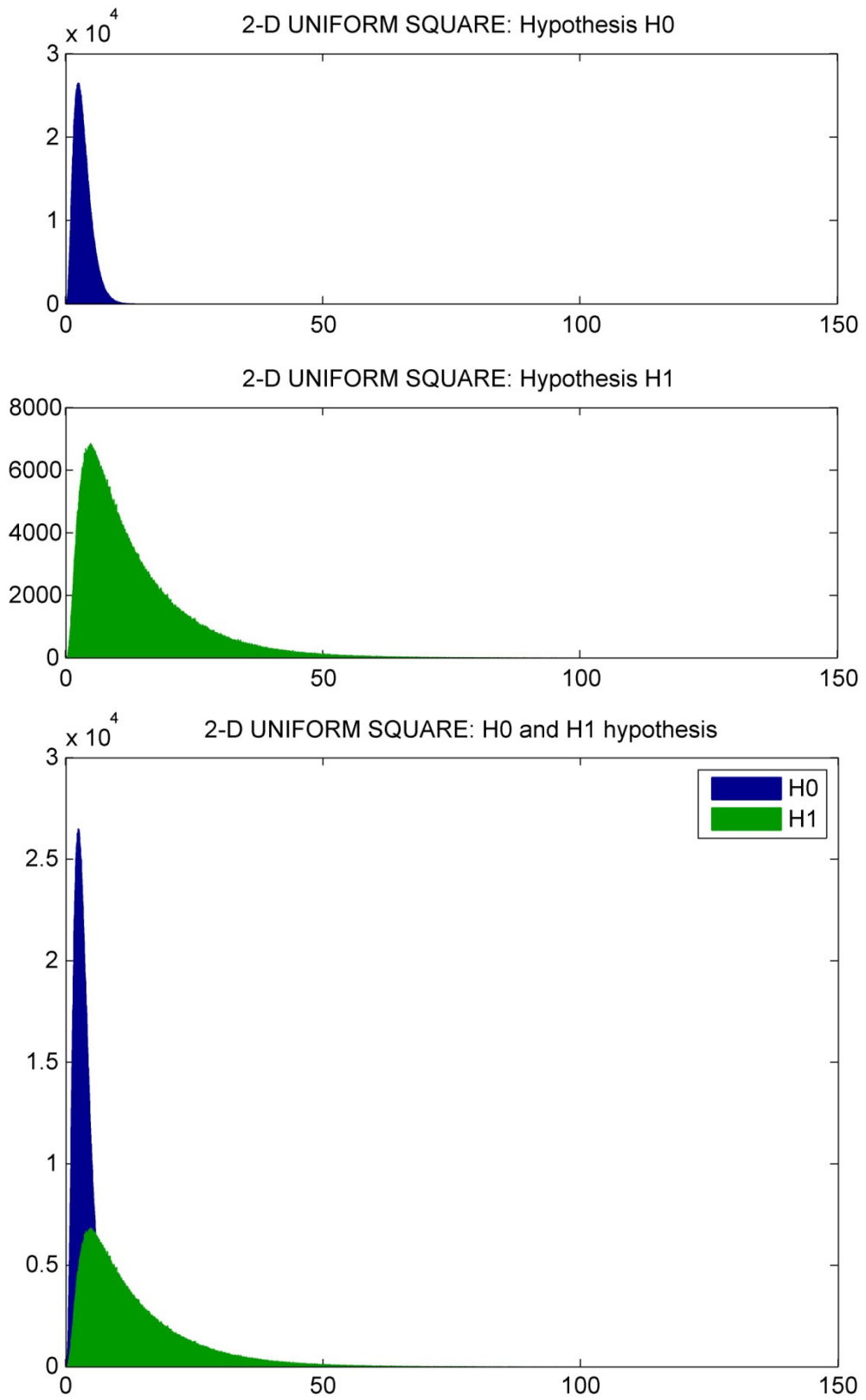Figure 3.11: 2-D Gaussian Hypothesis *H*0 and *H*1

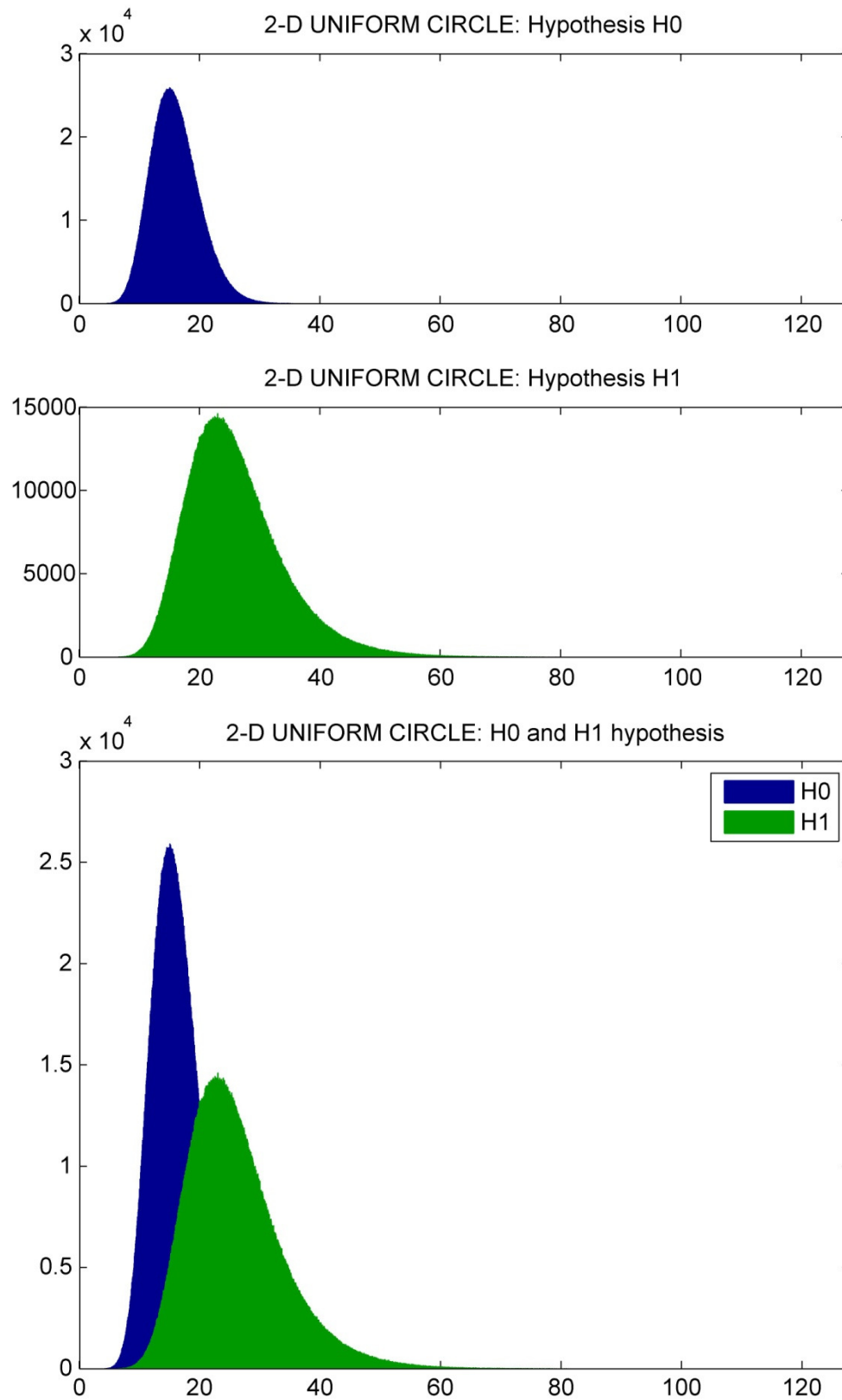Figure 3.12: 2-D Uniform Square Hypothesis *H*0 and *H*1
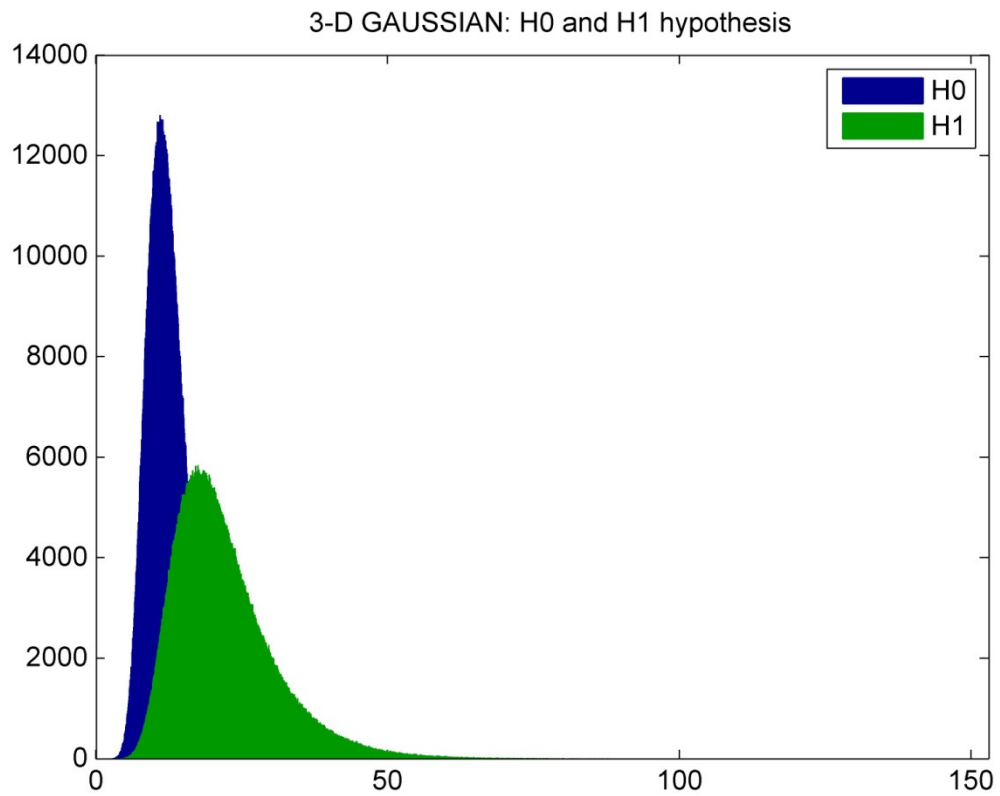
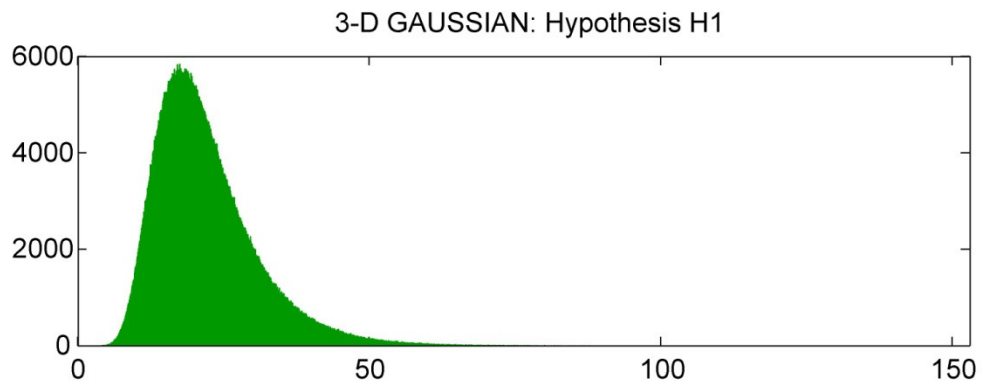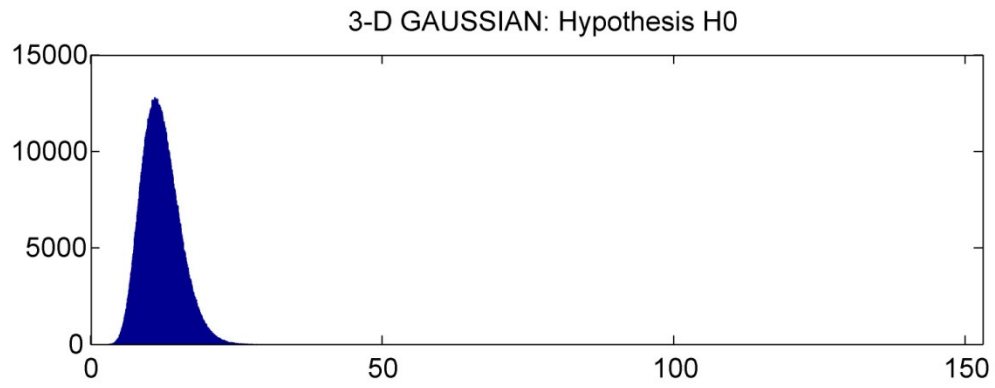Figure 3.13: 2-D Uniform Circle Hypothesis *H*0 and *H*1
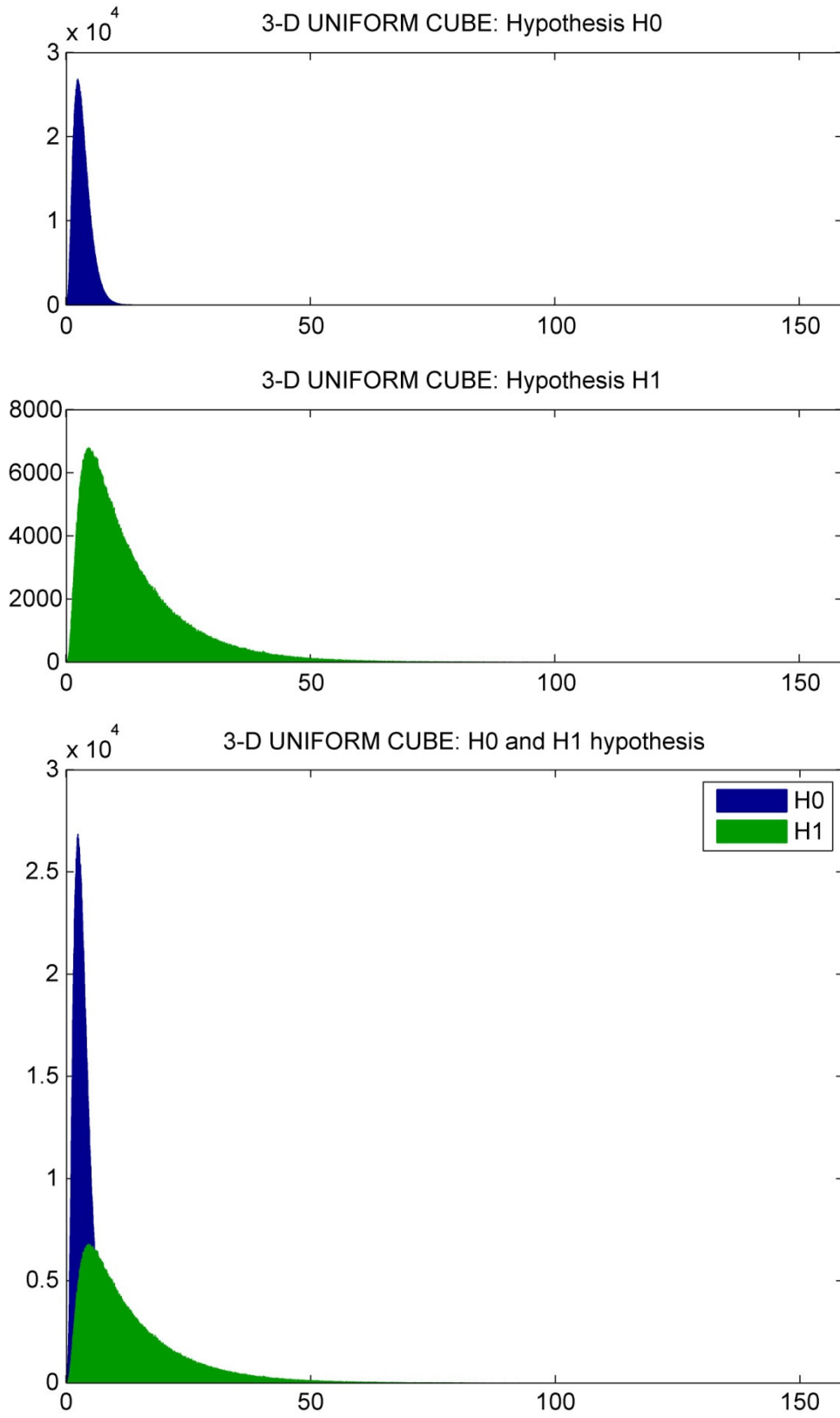
Figure 3.14: 3-D Gaussian Hypothesis *H*0 and *H*1

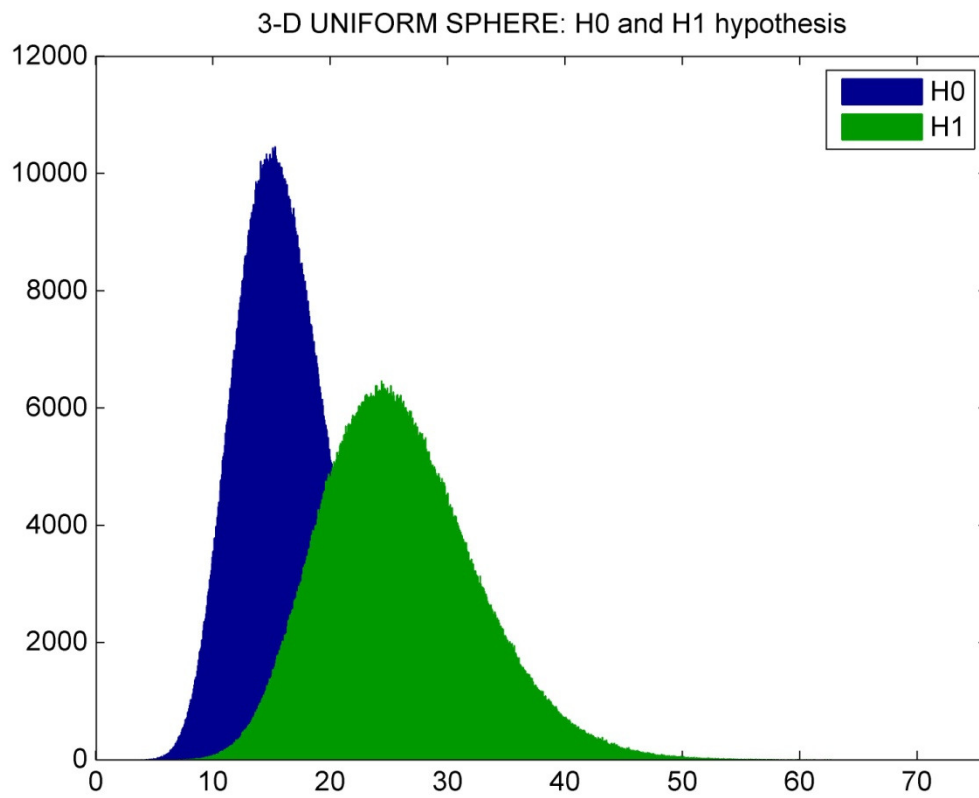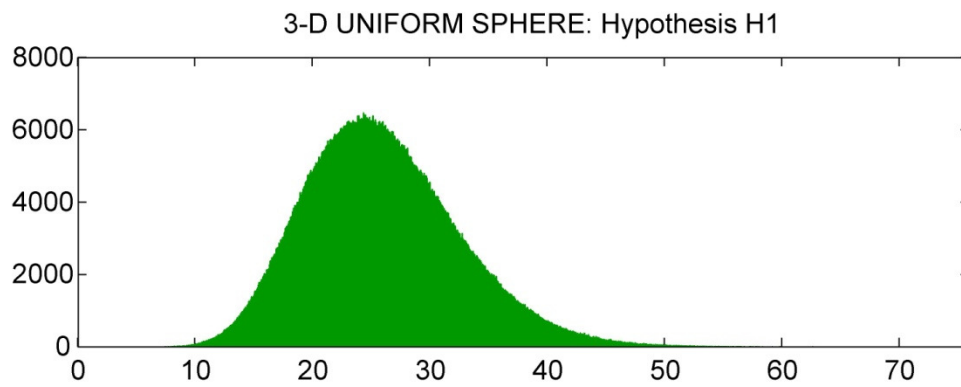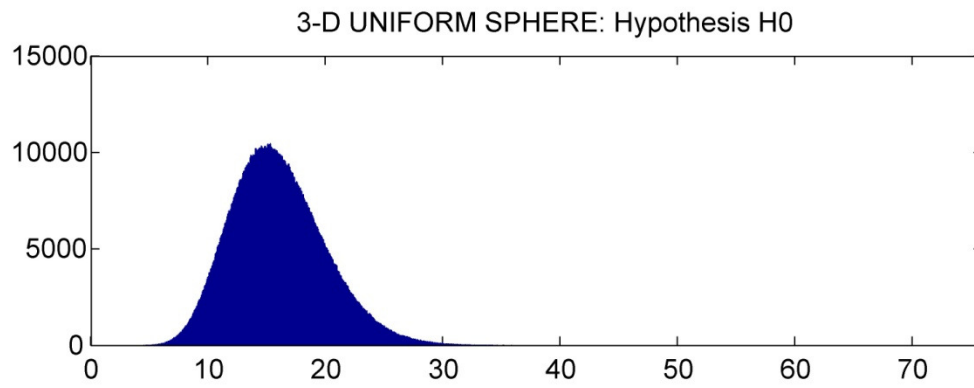Figure 3.15: 3-D Uniform Cube Hypothesis *H*0 and *H*1

Figure 3.16: 3-D Uniform Sphere Hypothesis *H*0 and *H*1

Chapter 4 ~ Results

In this chapter, we will focus on interpreting our data obtained from the previous chapter for the test statistics, **t** for the two hypotheses, *H*0 and *H*1. In addition, to be able to work with the six different target models, we have the option of varying the parameters below to observe the change in the performance of target detection.

- The spatial extent of the target (normalized by wavelength, λ).
- Signal-to-noise ratio (SNR) of the transmit signal.

For each of the criteria, we have generated plots which have been depicted in the sections to follow – first by holding the target extent constant fixed and altering SNR, and later reversing the process. It should be noted that the detector assumes the presence of a target and provides a statistical approach regarding its quality of performance.

4.1 Receiver Operator Characteristics (ROC)

For the first simulation batch, we want to observe the ROC curves for each model, of constant size 0.25λ, by varying the received signal SNR. Recall that SNR changes with respect to the scalar *α*, from equation 3.7 which has been assumed to be known. We then vary the discrimination threshold that sweeps through the density functions (shown in Figures 3.11 – 3.16) in the direction, shown in Figure 4.1, by the arrow.

As the thresholds sweeps from right to left, all points lying to the right of the threshold, under each hypothesis, are summed and stored in two different arrays. Each element in these arrays is then normalized by the total number of points present, which is a user input, under each density. For our convenience, the normalized elements under hypothesis *H*0 (shown in blue) are termed as the Probability of False Alarm (P_{FA}) and those under *H*1 (shown in green) as the Probability of Detection (P_D). The process is then repeated for a sequence of values of *α*, which alters the SNR of the received signals, to generate a series of different elements for both P_{FA} and P_D. Next we plot P_D against P_{FA} for varying SNR to produce a spectrum of ROC curves for each model. Figures 4.2 – 4.7 illustrates these ROC curves.

From these plots we notice that the axes have a maximum of *1* since each element of the target statistic under both *H*0 and *H*1 have been normalized. Each time we change the signal SNR, we obtain one ROC curve. For a lower SNR, the ROC curve is further away from the probability of detection (P_D) axis. Consequently, for a higher SNR value, the ROC curve will be closer to the P_D axis. We observe a similar pattern for the series of ROC curves shown below. Lower SNR-ROC curves are further away from the vertical axis, whereas higher SNR-ROC curves are skewed more towards the top-left portion of the plot, which is closer to the vertical (P_D) axis. From this phenomenon we can conclude that increasing the SNR of the signal yields better chances or target detection, or in other words, transmit signal selection have an influence on the detector performance.
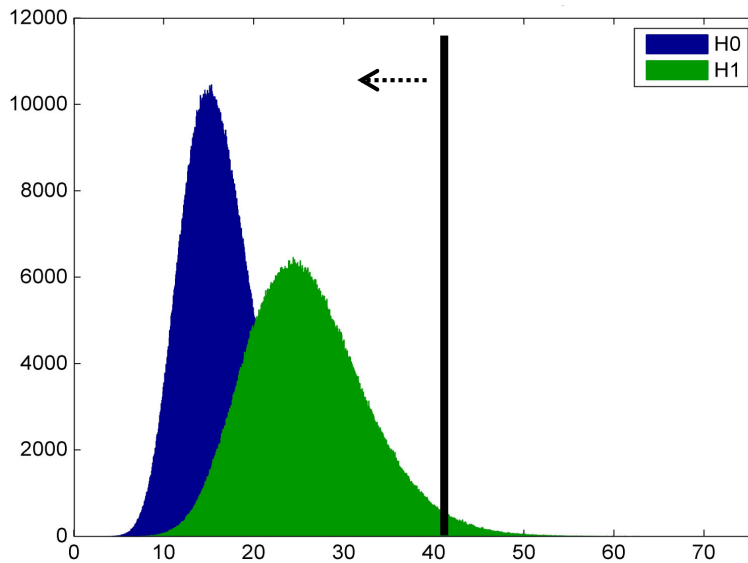

Figure 4.1: PDF and discrimination Threshold

The above procedure is repeated, but this time we vary the target extent keeping the SNR of the received signal constant. Similarly, we obtain a series of ROC curves which are shown in Appendix B. These plots convey similar information about the target detection performance, showing that increase in target extent provides higher probability of detecting a target. We have also used the Kullback–Leiber (KL) divergence to observe similar characteristic of the detector performance with increase in the target extent. The following section provides details about the KL divergence, and its implementation in target detection performance.
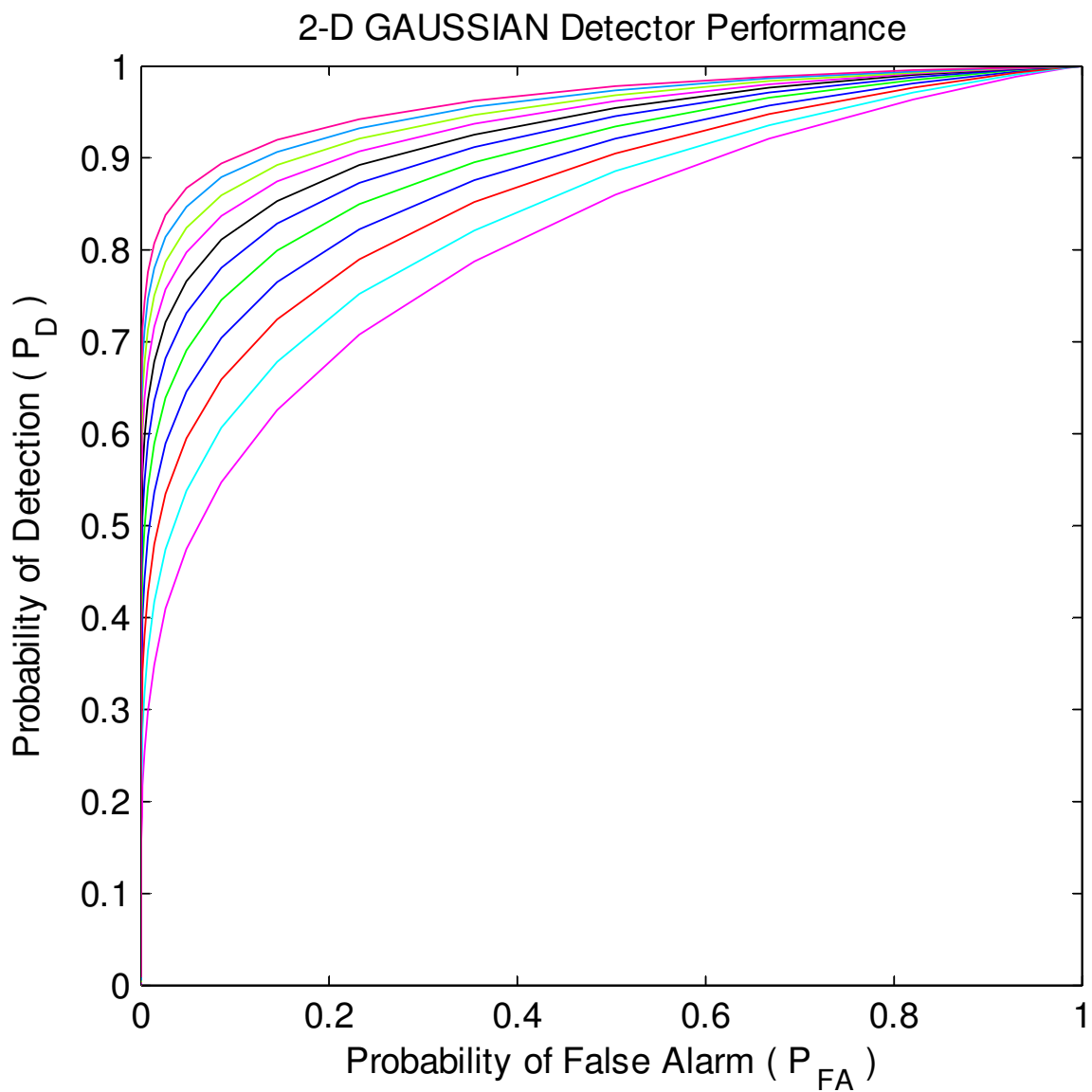
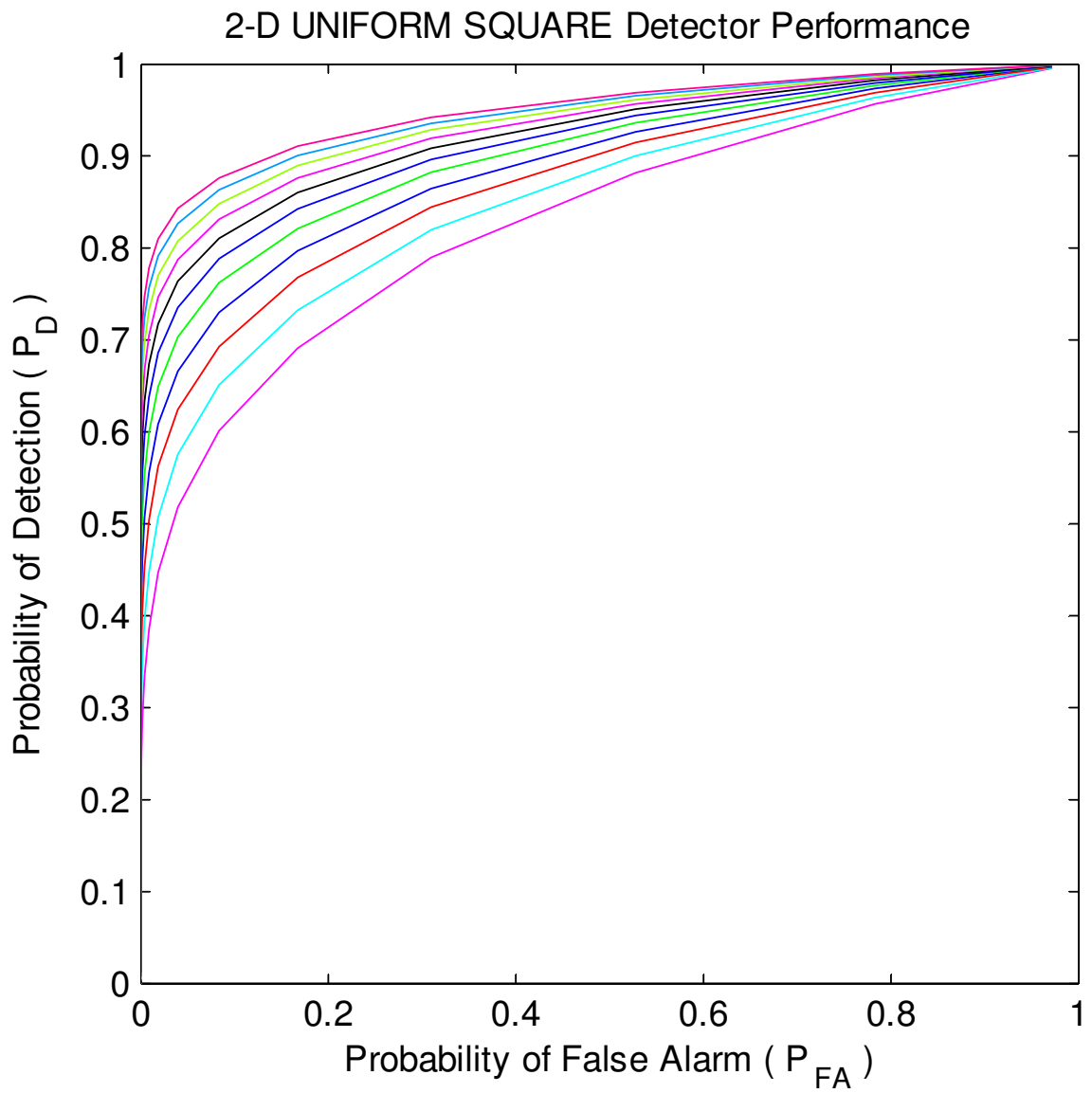Figure 4.2: ROC curve for 2-D Gaussian

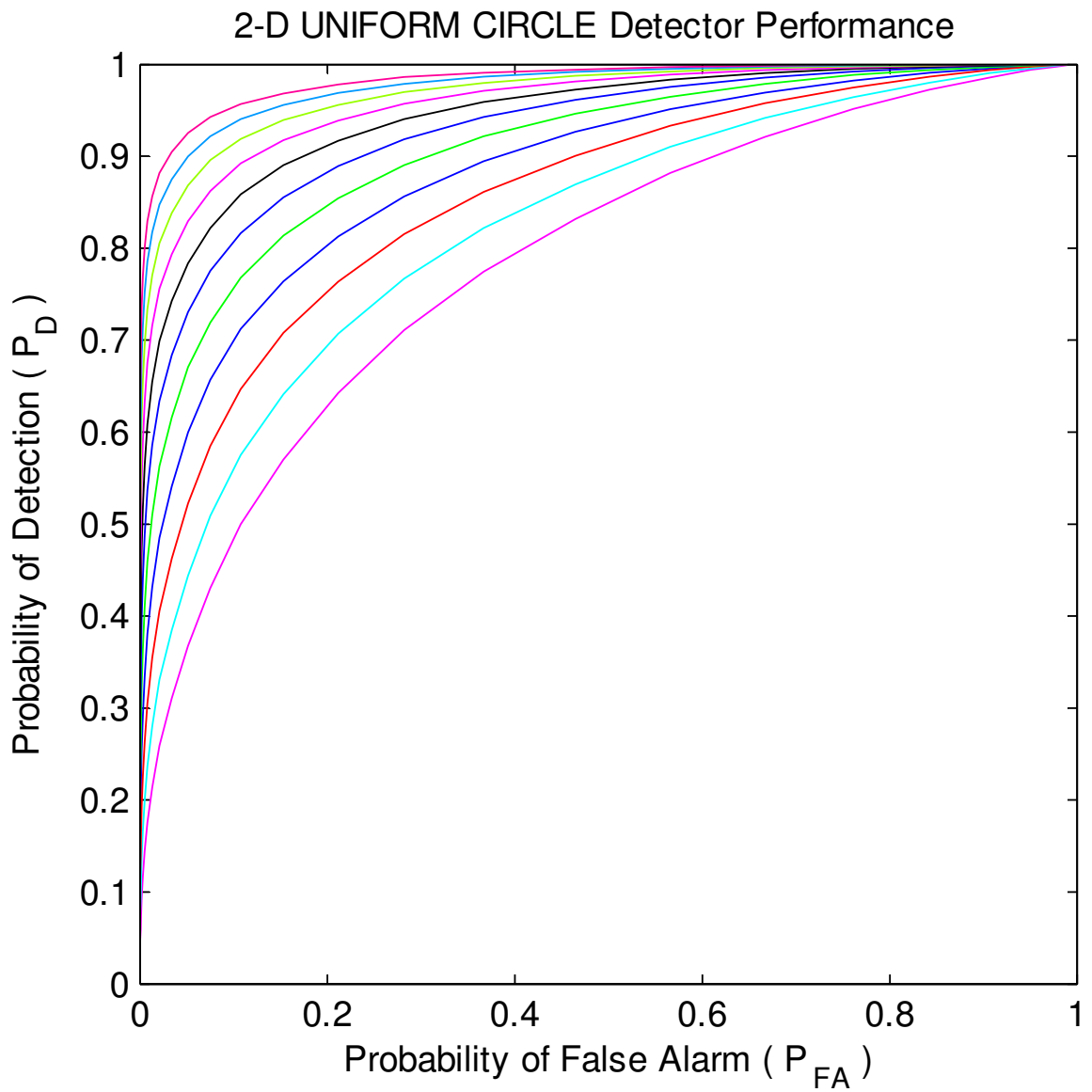Figure 4.3: ROC curve for 2-D Uniform Square

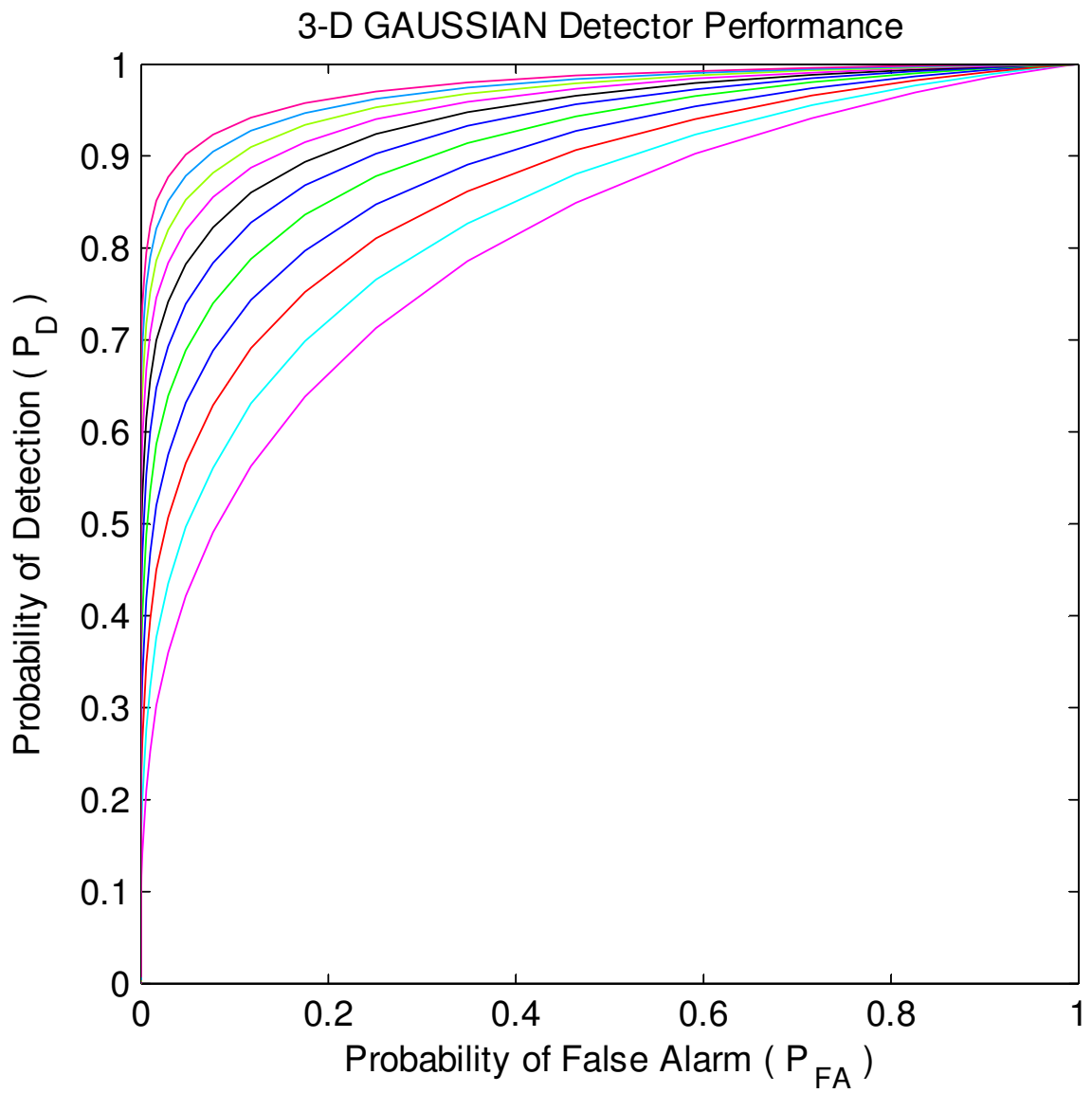Figure 4.4: ROC curve for 2-D Uniform Circle

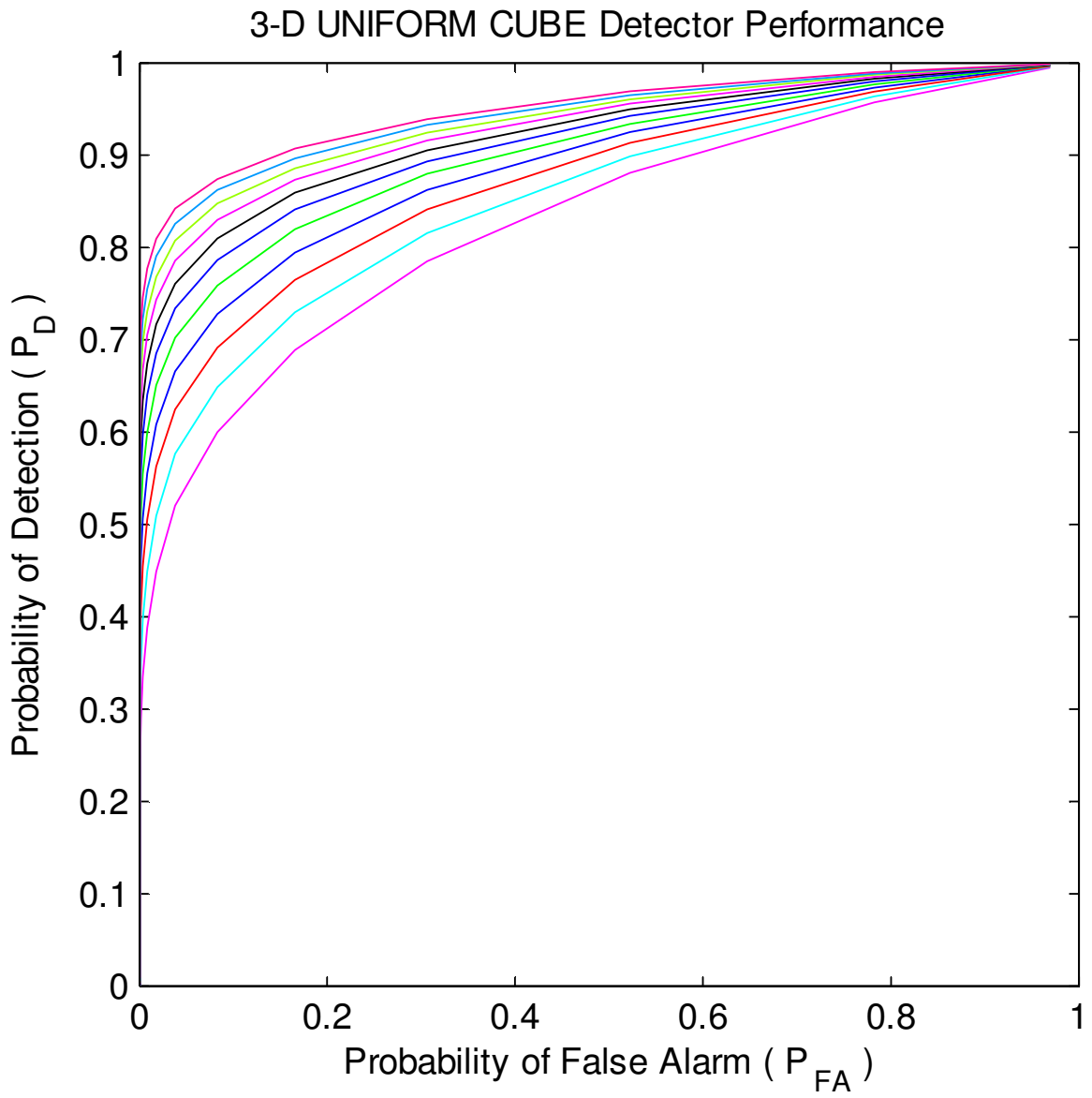Figure 4.5: ROC curve for 3-D Gaussian
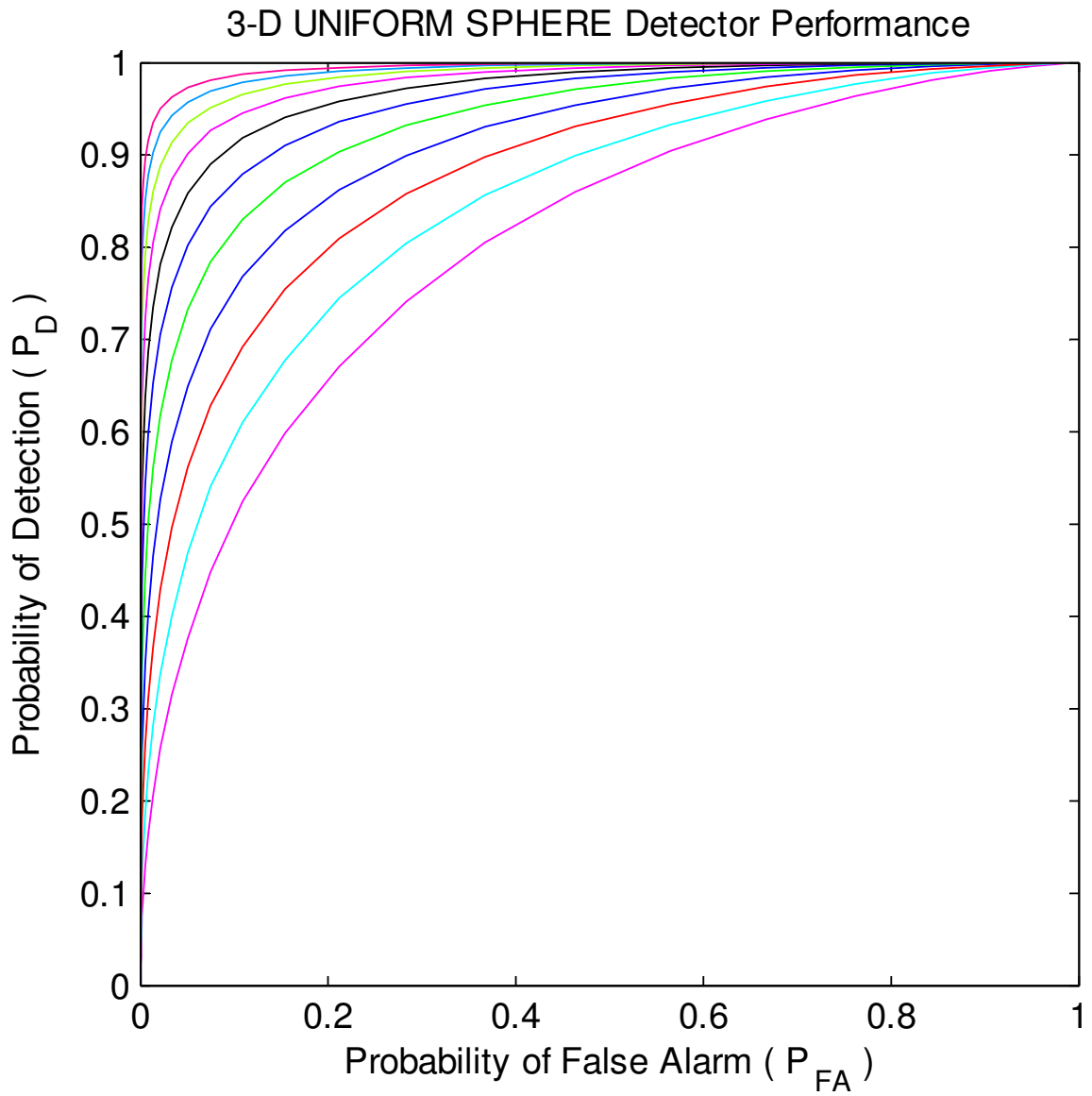
Figure 4.6: ROC curve for 3-D Uniform Cube

Figure 4.7: ROC curve for 3-D Uniform Sphere

4.2 Kullback–Leibler (KL) Divergence

In probability theory, KL divergence is a non-symmetric measure of divergence between two probability density functions P and Q. For the detector model, we have used the KL divergence to measure the approximate distance between density functions $H1$ and $H0$ (12, 23-25). The expression for KL divergence is given below

$$D_{KL}(P||Q) = -\sum_x p(x) \log_2 q(x) + \sum_x p(x) \log_2 p(x) \tag{4.1}$$

Substituting $H0$ for $p(x)$ and $H1$ for $q(x)$, we get

$$D_{KL}(P||Q) = -\sum_x p(H0) \log_2 q(H1) + \sum_x p(H0) \log_2 p(H0) \tag{4.2}$$

The KL divergence is always non-negative, so

$$D_{KL}(P||Q) \geq 0 \tag{4.3}$$

In order to preserve the symmetric nature of KL divergence (29,30) we perform

$$D_{KL}(P||Q) + D_{KL}(Q||P) \tag{4.4}$$

And for our detector model, this becomes

$$\left(-\sum_x p(H0) \log_2 q(H1) + \sum_x p(H0) \log_2 p(H0) \right)$$
$$+ \left(-\sum_x q(H1) \log_2 p(H0) + \sum_x q(H1) \log_2 q(H1) \right) \tag{4.5}$$

where, $p(H0)$ and $q(H1)$ are elements of the test statistics **t** for distributions $H0$ and $H1$ respectively, computed using equation 3.14. The above expression is the KL divergence scalar value indicating the approximate distance between the density functions. A series of divergence values are generated by varying the targets' sizes, in terms of wavelength λ, keeping SNR of received signal constant.

The plots in Figures 4.8 – 4.13 show the KL divergence against the target extent for each model. Each element for the KL divergence has been normalized in order to put

an upper limit of 1, which is what we see on the vertical axis of these plots. When the target extent is small, the KL divergence is less, referring to the fact that the hypotheses for $H0$ and $H1$ are not too far apart from each other. On the contrary, when the target is larger in size, the density functions for both $H0$ and $H1$ are further apart resulting in a larger value for the KL divergence. Extrapolating these phenomena we can say that if there is no target present, both $H0$ and $H1$ density functions will overlap making the KL divergence zero; and when the target is very big in size, the signals received at receiver end becomes more and more uncorrelated, and the KL divergence will be almost *1* due to the density functions being very far apart.

We observe similar pattern from the following plots for each target model. As the target extent increases, in terms of wavelength, the KL divergence increases accordingly which proves that the target extent have an impact on the performance of target detection. The bigger the target, the easier it is to detect. Appendix C illustrates similar phenomena, where SNR is altered, keeping the target extent constant for each model.
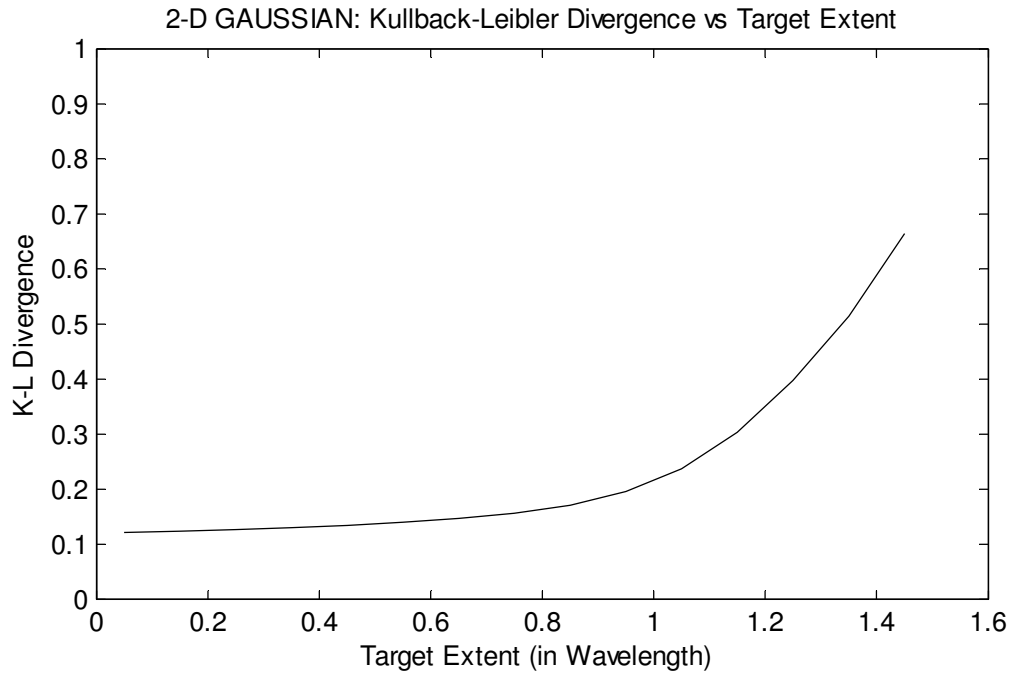
2-D GAUSSIAN: Kullback-Leibler Divergence vs Target Extent

Figure 4.8: KL divergence of 2-D Gaussian

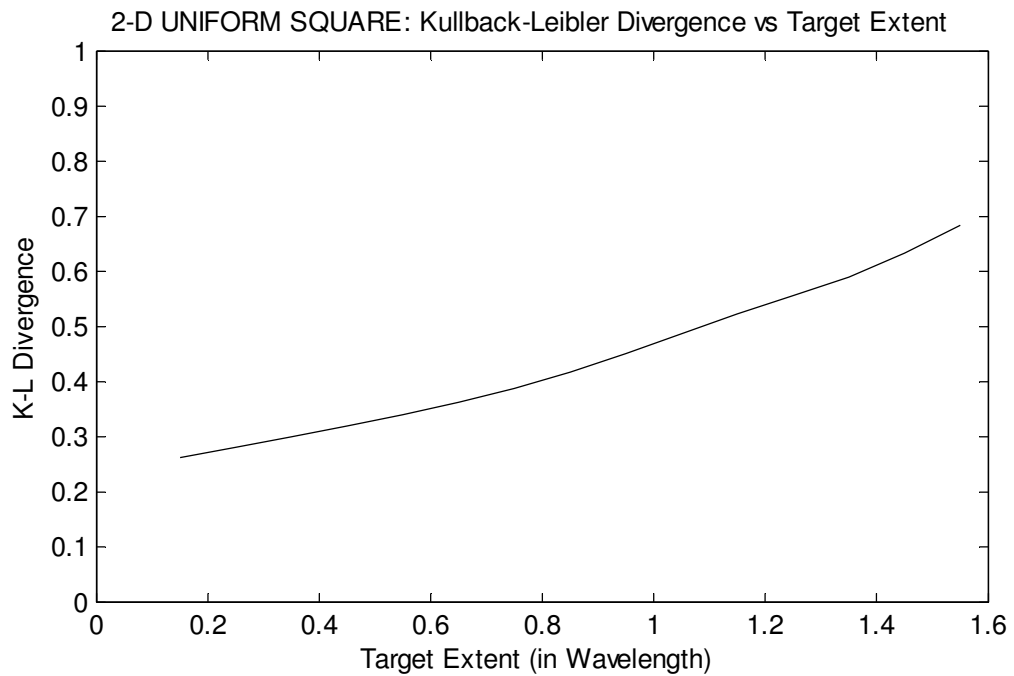2-D UNIFORM SQUARE: Kullback-Leibler Divergence vs Target Extent
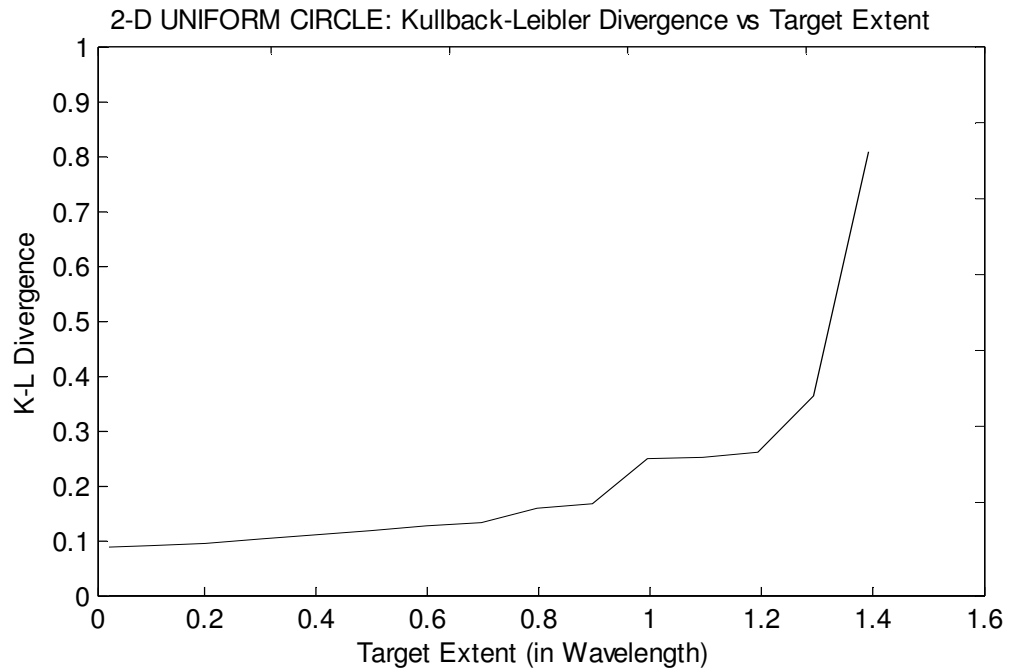
Figure 4.9: KL divergence of 2-D Uniform Square

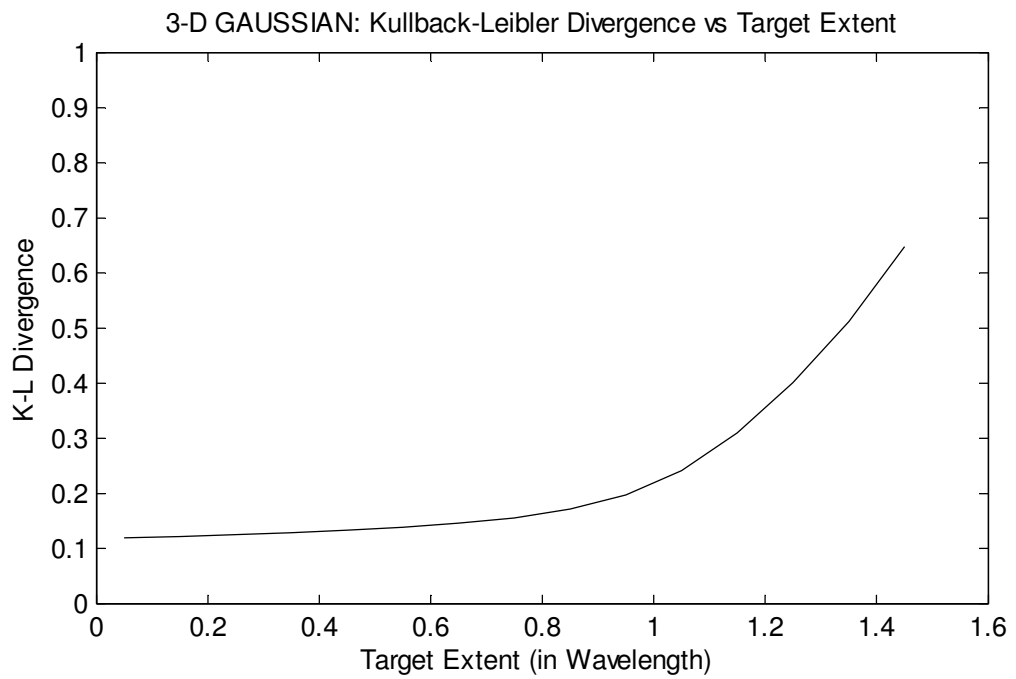Figure 4.10: KL divergence of 2-D Uniform Circle

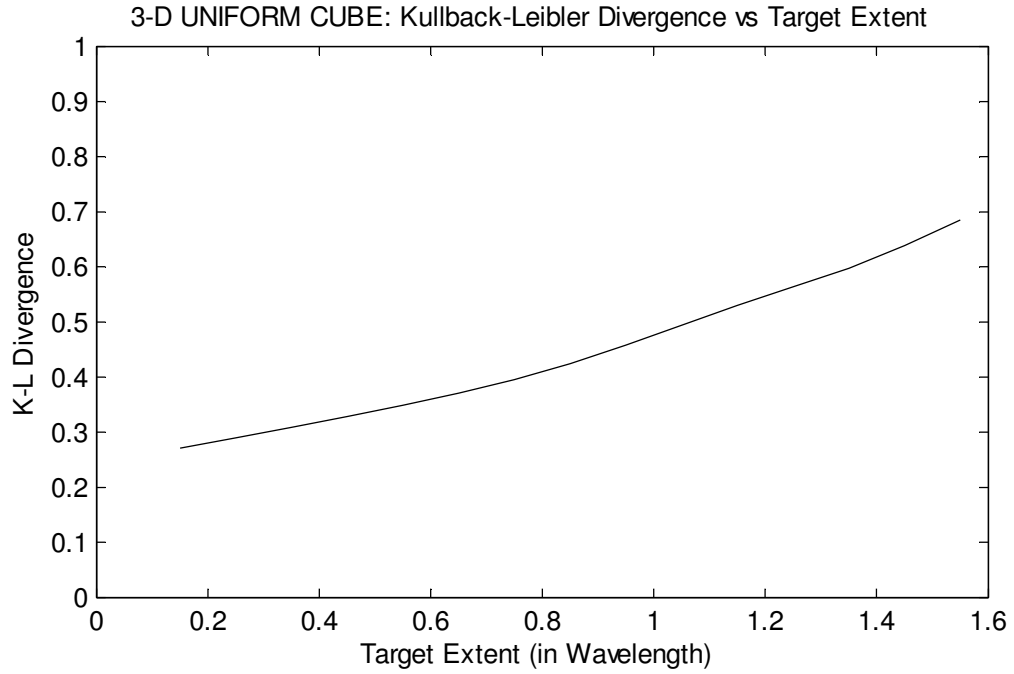Figure 4.11: KL divergence of 3-D Gaussian

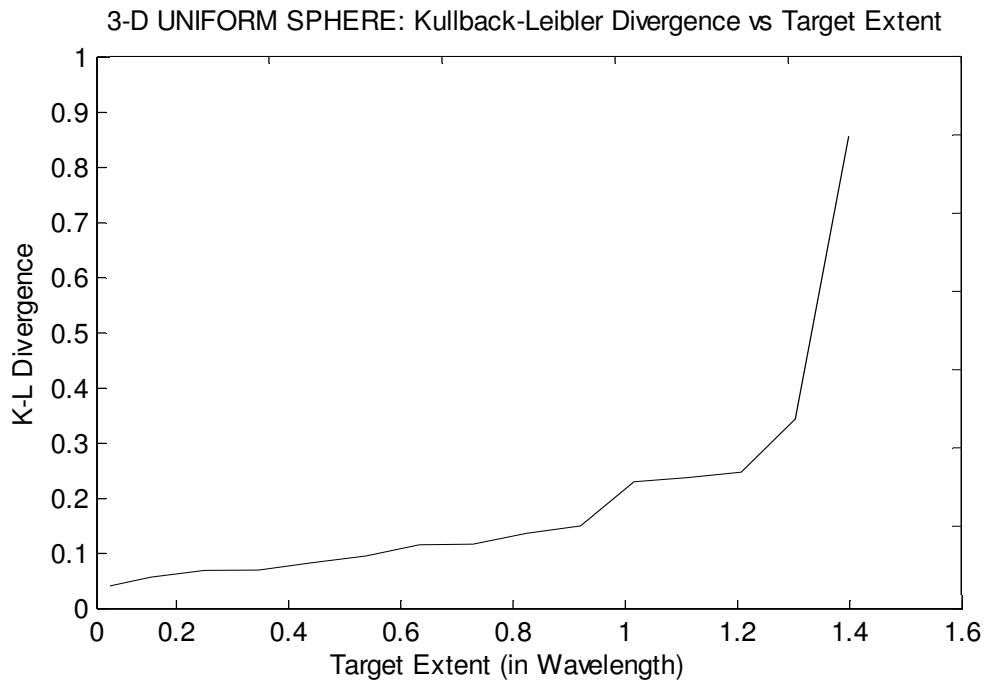Figure 4.12: KL divergence of 3-D Uniform Cube

Figure 4.13: KL divergence of 3-D Uniform Sphere

Chapter 5 ~ Recommendation & Future Work

5.1 Recommendation

In chapter 3 we mentioned that the scalar α, is assumed to be a known quantity and changing the numeric value of this scalar will alter the SNR of the received signal. If this value is not known, it will significantly change the test statistics for detector model. In the scenario where α is unknown, we have to estimate its value. A couple of ways this can be done, but both approaches will be numeric since a closed form solution may not be possible to obtain. From the equations (3.6 – 3.7) we can perform (14) the generalized likelihood ratio test (GLRT) for the scalar α, which will look as follows

$$\text{GLRT}_\alpha = \frac{\underset{\alpha}{max}\ F_1(\boldsymbol{y}; \alpha)}{F_0(\boldsymbol{y})} \tag{5.1}$$

Another approach to estimate α can be to

- Find the log-likelihood function from equations (3.8 – 3.9).
- Numerically compute the maximum likelihood of α.

In either ways once α is estimated, the test statistic will be more precise and the detector will have better quality in performance.

5.2 Future Work

The study and analysis conducted in this report brings forth scope for future some work. In the design of the detector, the following improvements are possible.

5.2.1 Time Delay in Transmitted Signal

For the detector we have used statistically independent signals, or orthogonal signals, that do not address the issue of time delays in reaching the target models from the transmitters. By using orthogonal signals, we have assumed that the signals are time aligned on the targets. This assumption was made primarily to simplify computation complexity. Potential work in this area would be to devise an algorithm to calculate time

delays between the transmitted signals and ensure that the received signals on the target models are time aligned.

5.2.2 Hypoexponential Distribution

The individual summand of the expression 3.14 are subject to an exponential distribution with mean α_k. Sum of independent exponential random variables with differing means α_k is said to have a *hypoexponential distribution*. When α_k are all distinct, the tail probabilities of the hypoexponential distribution are easily found using Laplace transform techniques. The hypotheses becomes

$$H0: \quad \alpha_k = \frac{\lambda_k}{1 + \lambda_k} \quad k = 1 \dots K \tag{5.2}$$

$$H1: \quad \alpha_k = \lambda_k \quad k = 1 \dots K \tag{5.3}$$

If the α_k are not distinct, cancellation of coefficients of the Laplace transforms is highly probable, which would result in cancellation of density functions, and consequently loss of information from the tail probabilities. Potential work in this area would be to compute tail probabilities of hypoexponential distribution by ensuring that no cancellation of coefficients occurs. By developing a power series for the Laplace domain, this problem can be avoided to a great extent.

5.2.3 Adaptive Sensing of Detection

The spatial diversity MIMO radar model provides with a new problem to this well-known dichotomy between coherent and noncoherent processing, *i.e.* what one does with the received data after the additive white noise is included. With an active sensing modality like radar, we have the opportunity to influence the statistics of the received data before the effects of the noise, through the choice of the signal matrix **S**. One can transmit highly correlated signals thus achieving a high SNR gain on the target model, or one can transmit uncorrelated signals, thus illuminating the different aspects of the target in different ways. This is the analogue of coherent *vs.* noncoherent processing, on the transmit side of the problem (9,10,13). Here we have an analogous detection problem, where the data model becomes

$$\mathbf{y} = \mathbf{Sh} + \mathbf{w} \tag{5.4}$$

and one needs to choose between the presence ($\mathbf{h} \neq 0$) or absence ($\mathbf{h} = 0$) of the target. The question then becomes, how does one choose $\mathbf{S}$ to maximize probability of detection or some other appropriate parametric metric.

Furthermore, with the appropriate processing of the data, the data vector can be written as,

$$\mathbf{v} = \Sigma\mathbf{u} + \mathbf{n} \tag{5.5}$$

where, $\mathbf{u}$ is the matrix of K independent target components with variances λ_k, and effect of the signal matrix is summarized in the diagonal matrix Σ whose diagonal elements σ_k are subject to the energy constraint

$$E = \sum_{k=1}^{K} \sigma_k^2 \tag{5.6}$$

The problem then becomes a choice of how to illuminate the component of $\mathbf{u}$ to create the best detector. The general solution to this adaptive sensing for detection problem is open to further work. However, the solutions for two extreme cases, corresponding to coherent and noncoherent detection, are readily available.

Chapter 6 ~ Conclusion

In this report we have presented a total of six examples of 2-D and 3-D complex point target models. They are 2-D Gaussian, 2-D Uniform Square, 2-D Uniform Circle, 3-D Gaussian, 3-D Uniform Cube, and 3-D Uniform Sphere. The MATLAB GUI toolbox provides the user with the option to change the target extent and number of scatterers accordingly. Monostatic and bistatic radar models are simulated in the toolbox to show the target reflectivity.

These targets models were incorporated into a MIMO Radar signal data for target detection. The MIMO system setup had four transmitters and four receivers, and the target is assumed to be at the center of our coordinate system. Complex reflectivity for each pair of bistatic view angle was computed to obtain information about the RCS of the targets. The correlation function for each of the models is mathematically derived, which are then used to compute the covariance matrix. The resulting hypothesis testing problem turns into a Gauss-Gauss detection problem. Statistically independent or, orthogonal signals were received by the targets to provide us with the convenience of assuming that these received signals are time aligned. This is a non-trivial assumption made to reduce mathematical complexity as it portrays a significant technical challenge in its own rights, something that can be looked into for future work following this project.

We looked at the Eigenvalue distributions for each model, which appeared to be similar as expected. As the target extent becomes significantly large, these distributions tend to be uniform in nature suggesting that signals at the receiver became uncorrelated. The test statistic for the detection problem is generated, followed by histograms of the density functions for noise-only case ($H0$) and signal/target present case ($H1$). For both the hypothesis we have assumed that a scalar, α is known which is primarily responsible for governing the SNR of the system. In the case where we do not know α, we need to estimate it using methods proposed in the previous chapter.

At this stage, we have a detector ready. We then intend to show that the target parameters and transmit signal selection have an influence on the detector performance

through SNR. Based on the test statistic generated, empirical ROC curves are produced for each target model. Elements lying under hypothesis $H1$ will reflect the probability of detecting the target (P_D). And elements under $H0$ can be assumed to be noise and so are termed as the probability of false alarm (P_{FA}) for a fixed target extent. The procedure is repeated keeping the target extent constant and altering the SNR of the received signals, and results displayed by means of Kullback–Leibler (KL) divergence to make it visually intensive to depict more information about the detector.

From the ROC curves and KL divergence plots, we can confirm that selection of transmit signals and target parameter/size noticeably influence the detector performance respectively. To reassure the claim we have generated additional figures in Appendix B and Appendix C, where we repeat the procedures by reversing the parameter constraints. Appendix B provides a sequence of ROC curves that are generated for varying target extent keeping SNR constant. Appendix C shows the KL divergence plots of all the six models for changing SNR values, with the target extent remaining the same.

References

[1] J. Li, and P. Stoica, *MIMO Radar Signal Processing*, Wiley – IEEE Press, 2008.

[2] E. Fishler, A. Haimovich, R.S. Blum, L.J. Cimini, D. Chizhik, and R. Valenzuela, "Spatial Diversity in Radars – Models and Detection Performance," *IEEE Trans. Signal Processing*, vol. 54, no. 3, p. 823-838, March 2006.

[3] R. DeLano, "Theory of Target Glint or Angular Scintillation in Radar Tracking," *Proc. IRE*, vol. 41, no. 12, p. 1778-1784, December 1953.

[4] J. Dunn, D. Howard, and A. King, "Phenomena of Scintillation Noise in Radar Tracking System," *Proc. IRE*, vol. 47, no. 5, p. 855-863, May 1959.

[5] L. Peters, and F. Weimer, "Tracking Radar for Complex Targets," *Proc IEE*, vol. 110, no. 12, p. 2149-2162, December 1963

[6] R. Ostrovityanov, and F. Basalov, *Statistical Theory of Extended Radar Targets*, Artech House, 1985, 364 p.

[7] Z. Zhang, and D.R. Fuhrmann, "Complex Point Target Models for Multistatic Radar," *Proc. 42nd Asilomar Conf. Signals, Systems, and Computers*, Pacific Grove, CA, October 2008.

[8] C. Chen, and P.P. Vaidyanathan, "MIMO Radar Space-Time Adaptive Processing using Prolate Spheroidal Wave Functions," *IEEE Trans. on Signal Processing*, vol. 56, p. 623-635, January 2008.

[9] C. Helstrom, *Elements of Signal Detection and Estimation*, 1st ed., Prentice Hall, 1994, 586 p.

[10] L. Scharf, "Invariant Gauss-Gauss Detection," *IEEE Trans. Information Theory*, vol. 19, no. 4, p. 422-427, July 1973.

[11] K.S. Trivedi, *Probability and Statistics with Reliability, Queueing, and Computer Science Applications*, 2nd ed., Wiley-Interscience, 2002, 830 p.

[12] M. Bell, "Information Theory and Radar Wave Design," *IEEE Trans. Information Theory*, vol. 39, no. 5, p. 1578-1597, September 1993.

[13] D.R. Fuhrmann, and G. San Antonio, "Transmit Beamforming for MIMO Radar Systems using Signal Cross-correlation," *IEEE Trans. Aerospace and Electronic Systems*, vol. 44, no. 1, p 1-16, January 2008.

[14] O. Zeitouni, J. Ziv, and N. Merhav, "When is Generalized Likelihood Ratio Test Optimal," *IEEE Intl. Symposium on Information Theory*, vol. 38, p. 1597-1602, September 2002.

[15] A. Papoulis, and S.U. Pillai, *Probability, Random Variables and Stochastic Processes*, 4th ed., McGraw Hill Higher Education, 2002, 852 p.

[16] M.S. Gockenbach, *Finite-Dimensional Linear Algebra*, 1st ed., CRC Press, 2010, 672 p.

[17] S.M. Kay, *Fundamentals of Statistical Signal Processing, Volume I: Estimation Theory*, 1st ed., Prentice Hall, 1993, 625 p.

[18] S.M. Kay, *Fundamentals of Statistical Signal Processing, Volume II: Detection Theory*, 1st ed., Prentice Hall, 1998, 672 p.

[19] J.J. Zhang, and A.P. Suppappola, "MIMO Radar with Frequency Diversity," *Intl. WD&D Conf.*, p. 208-212, April 2009.

[20] E. Weisstein, *Bessel Function of the First Kind*, from MathWorld, A Wolfram Web Resource, 2009, http://mathworld.wolfram.com

[21] E. Weisstein, *Jinc Function*, from MathWorld, A Wolfram Web Resource, 2009, http://mathworld.wolfram.com

[22] E. Weisstein, *Spherical Bessel Function of the First Kind*, from MathWorld, A Wolfram Web Resource, 2009, http://mathworld.wolfram.com

[23] J. Shlens, *Notes on the Kullback-Leibler Divergence and Likelihood Theory*, Salk Institute for Biological Studies, La Jolla, CA, August 2007

[24] F.P. Cruz, "Kullback-Leibler Divergence Estimation of Continuous Distributions," *IEEE Intl. Symposium on Information Theory*, p. 1666-1670, August 2008.

[25] J.R. Hershey, and P.A. Olsen, "Approximating the Kullback-Leibler Divergence between Gaussian Mixture Models," *IEEE Intl. Conf. on Acoustics, Speech, and Signal Processing*, p. 317-320, Honolulu, HI, April 2007.

[26] A.M. Haimovich, R.S. Blum, and L.J. Cimini, "MIMO Radar with Widely Separated Antennas," *IEEE Signal Processing Mag.*, p. 116-129, January 2008.

[27] E. Fishler, A. Haimovich, R. Blum, L. Cimini, D. Chizhik, and R. Valenzuela, "MIMO radar: An idea whose time has come," *IEEE International Conf. Radar*, Philadelphia, PA, April 2004.

[28] E. Fishler, A. Haimovich, R. Blum, L. Cimini, D. Chizhik, and R. Valenzuela, "Statistical MIMO Radar," *12th Conf. on Adaptive Sensors Array Processing*, Lexington, MA, March 2004.

[29] A.K. Seghouane, and S.I. Amari, "The AIC Criterion and Symmetrizing Kullback-Leibler Divergence," *IEEE Trans. on Neural Networks*, p. 97-106, January 2007.

[30] D. Johnson, and S. Sinanovic, "Symmetrizing the Kullback-Leibler Divergence," *IEEE Trans. on Information Theory*, March 2001.

Appendix A ~ Reflectivity Correlation
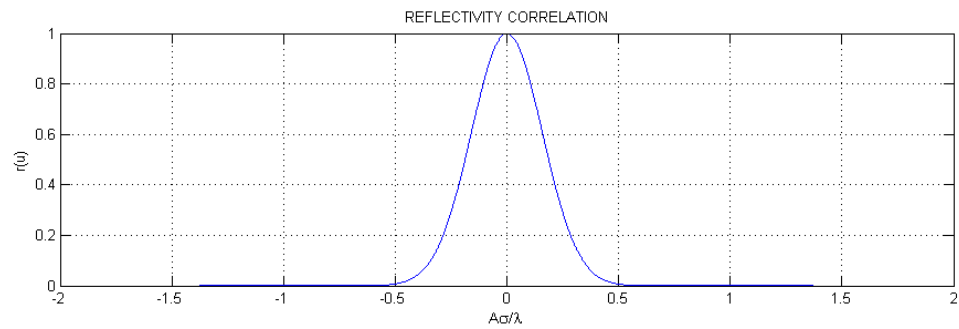
Figure A.1: Reflectivity Correlation for 2-D Gaussian
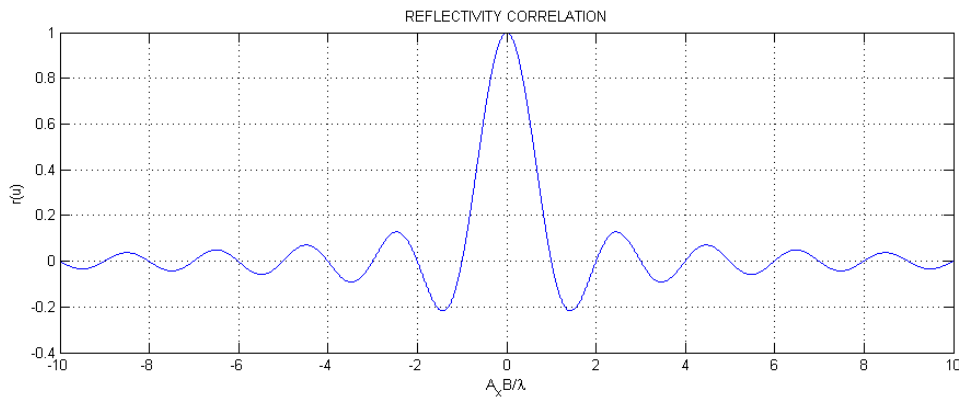
Figure A.2: Reflectivity Correlation for 2-D Uniform Square
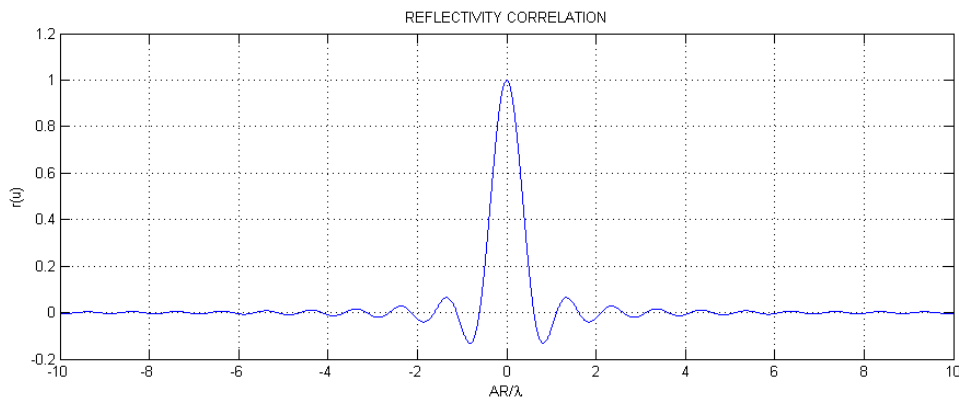
Figure A.3: Reflectivity Correlation for 2-D Uniform Cube
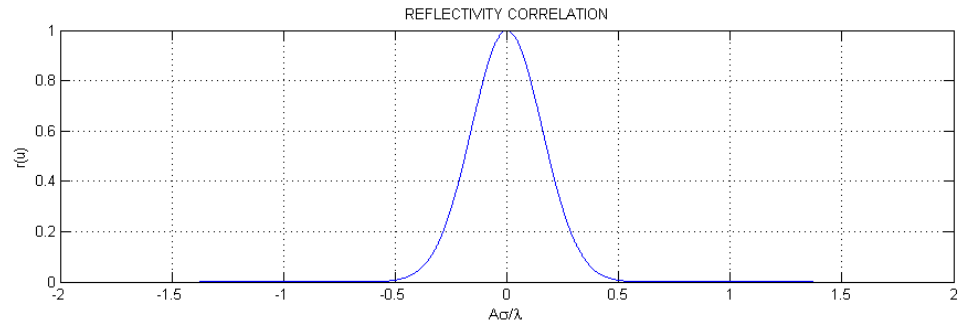
Figure A.4: Reflectivity Correlation for 3-D Gaussian
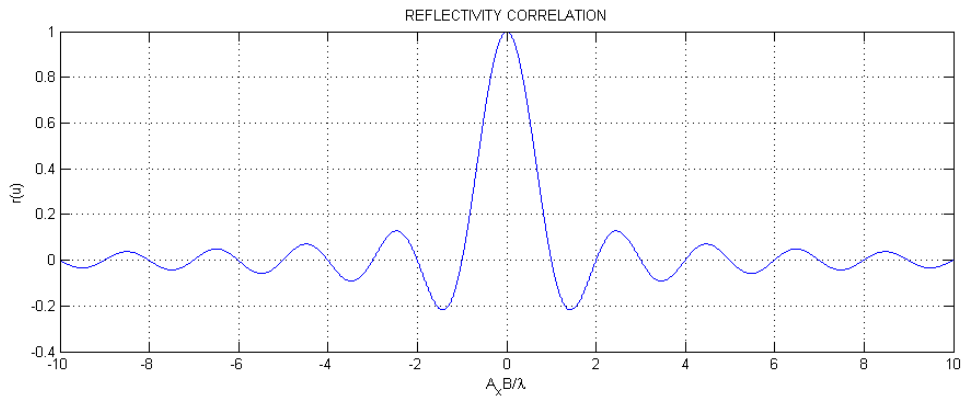
Figure A.5: Reflectivity Correlation for 3-D Uniform Cube
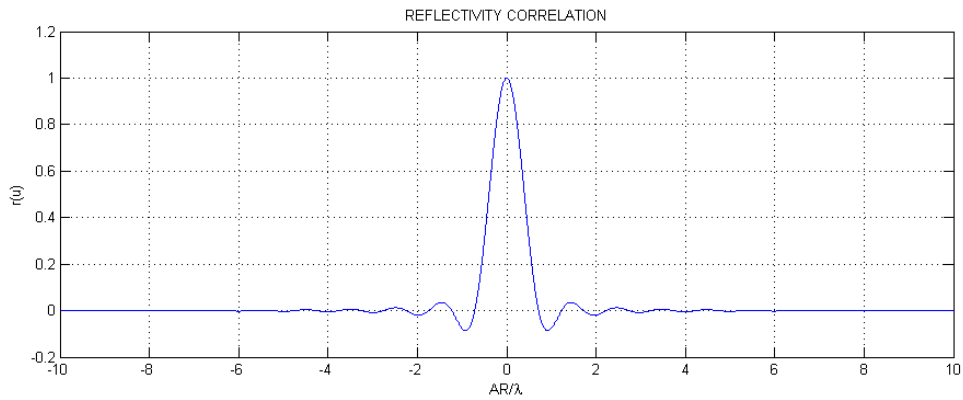
Figure A.6: Reflectivity Correlation for 3-D Uniform Sphere

Appendix B ~ Detector Performance 1

ROC curves for target models with fixed SNR, and varying target size
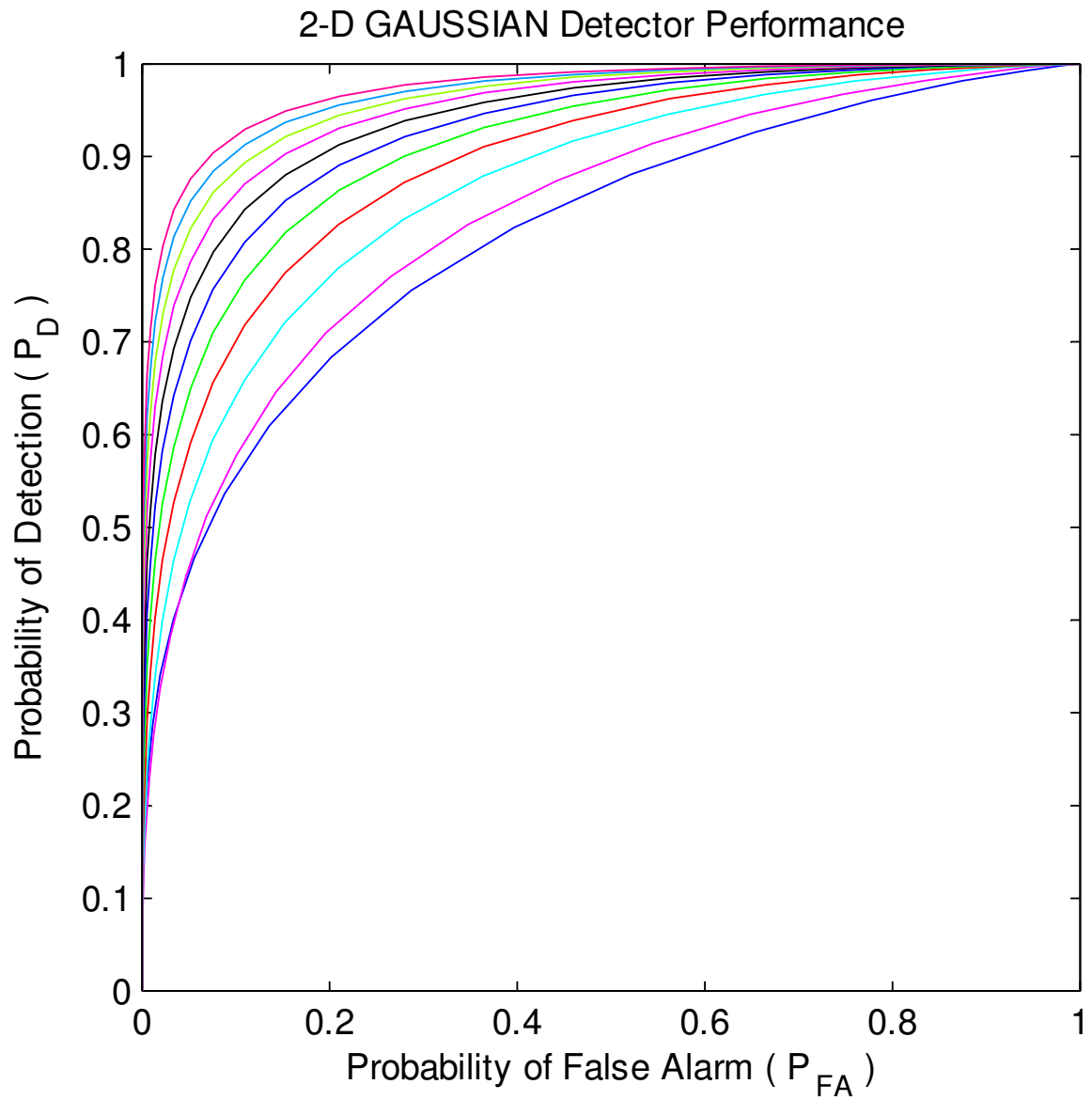
Figure B.1: ROC plot for 2-D Gaussian, for fixed SNR
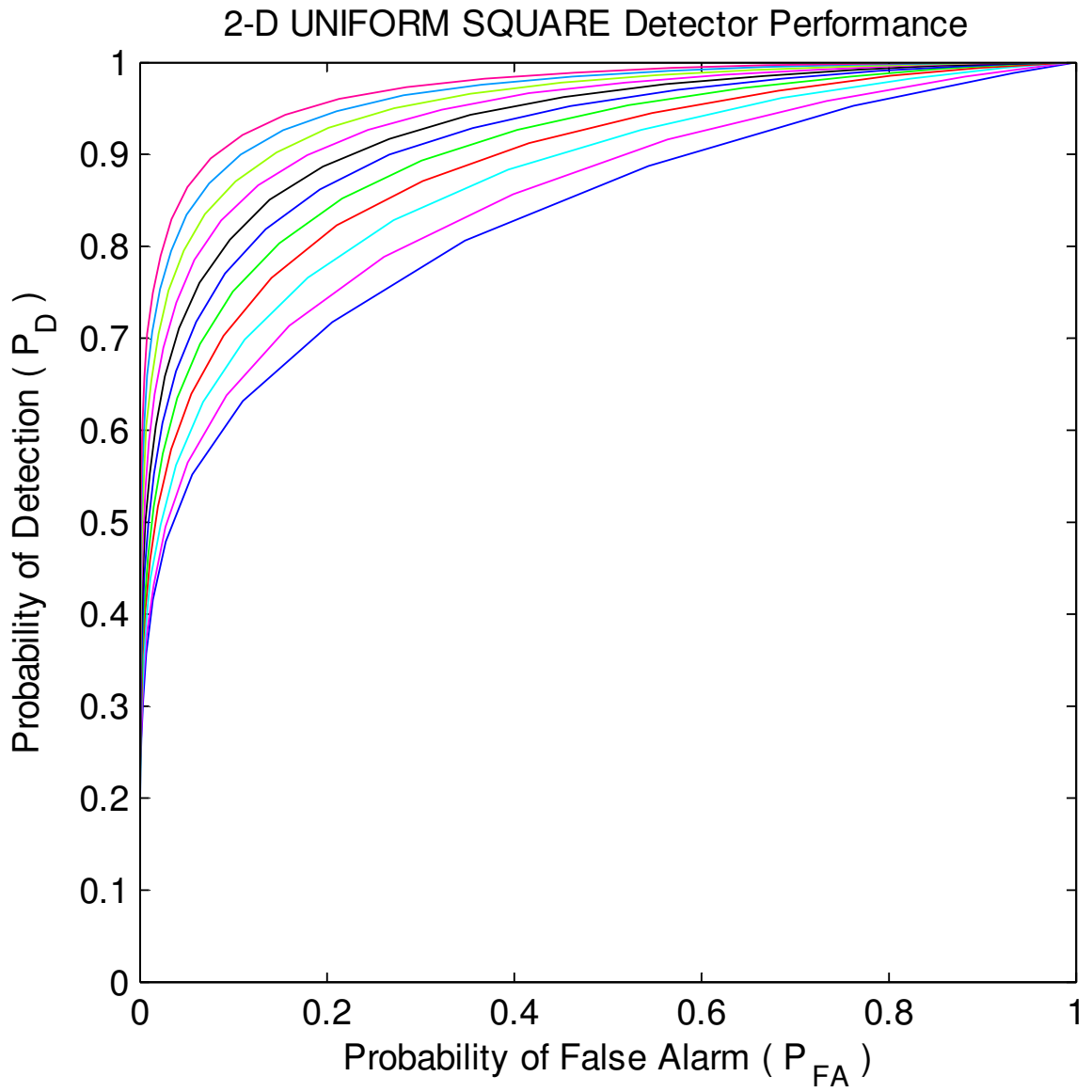
Figure B.1: ROC plot for 2-D Uniform Square, for fixed SNR
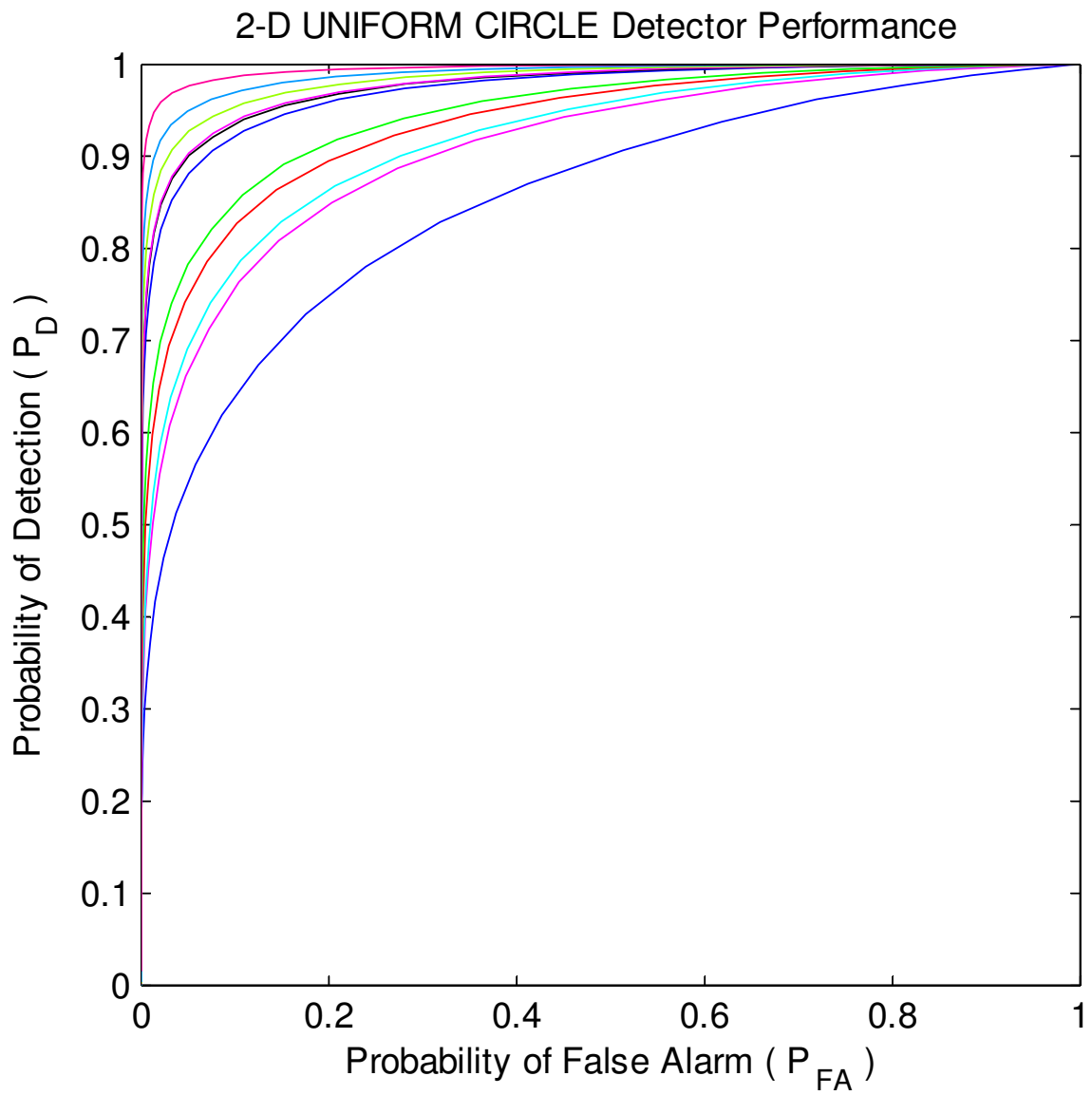
Figure B.3: ROC plot for 2-D Uniform Circle, for fixed SNR
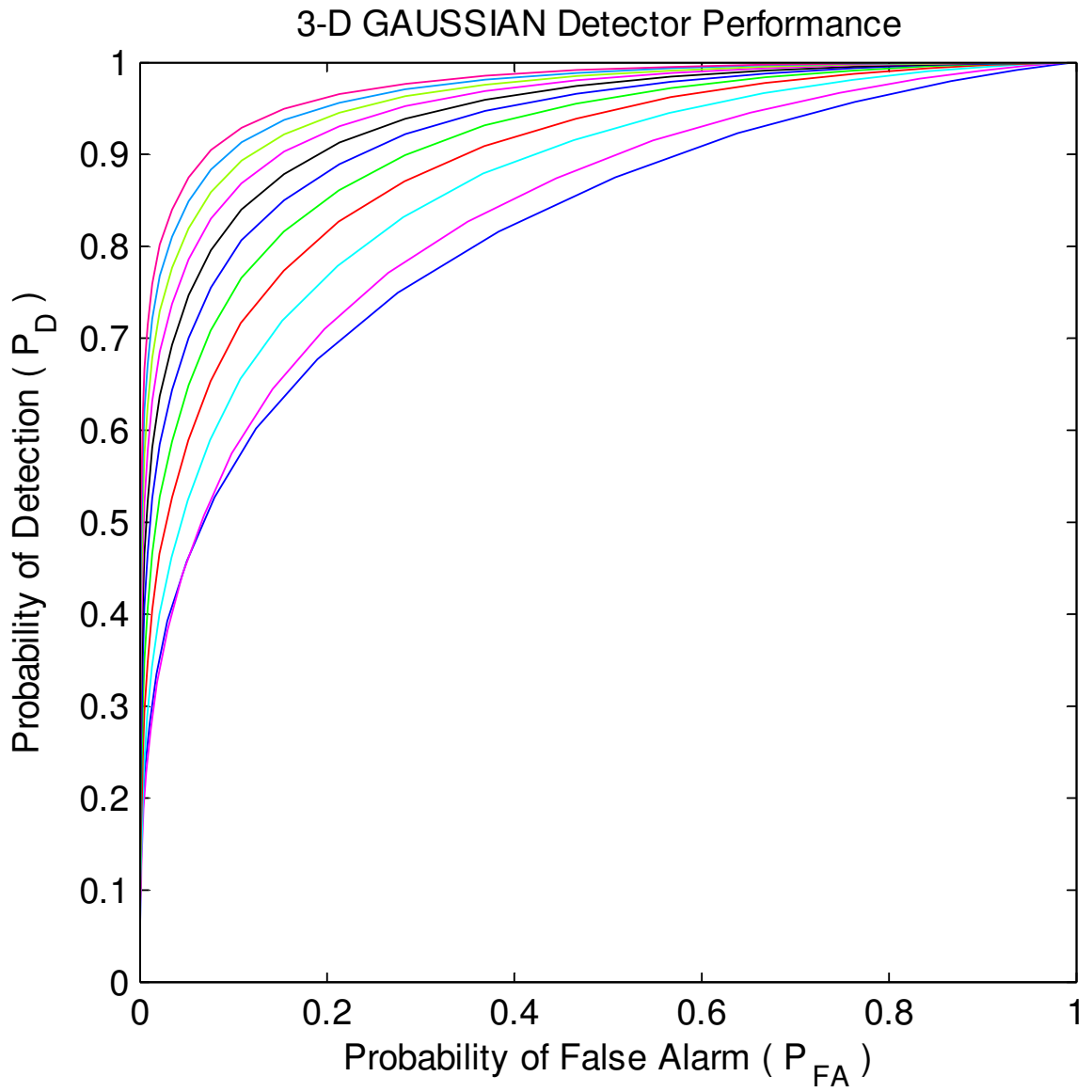
Figure B.4: ROC plot for 3-D Gaussian, for fixed SNR
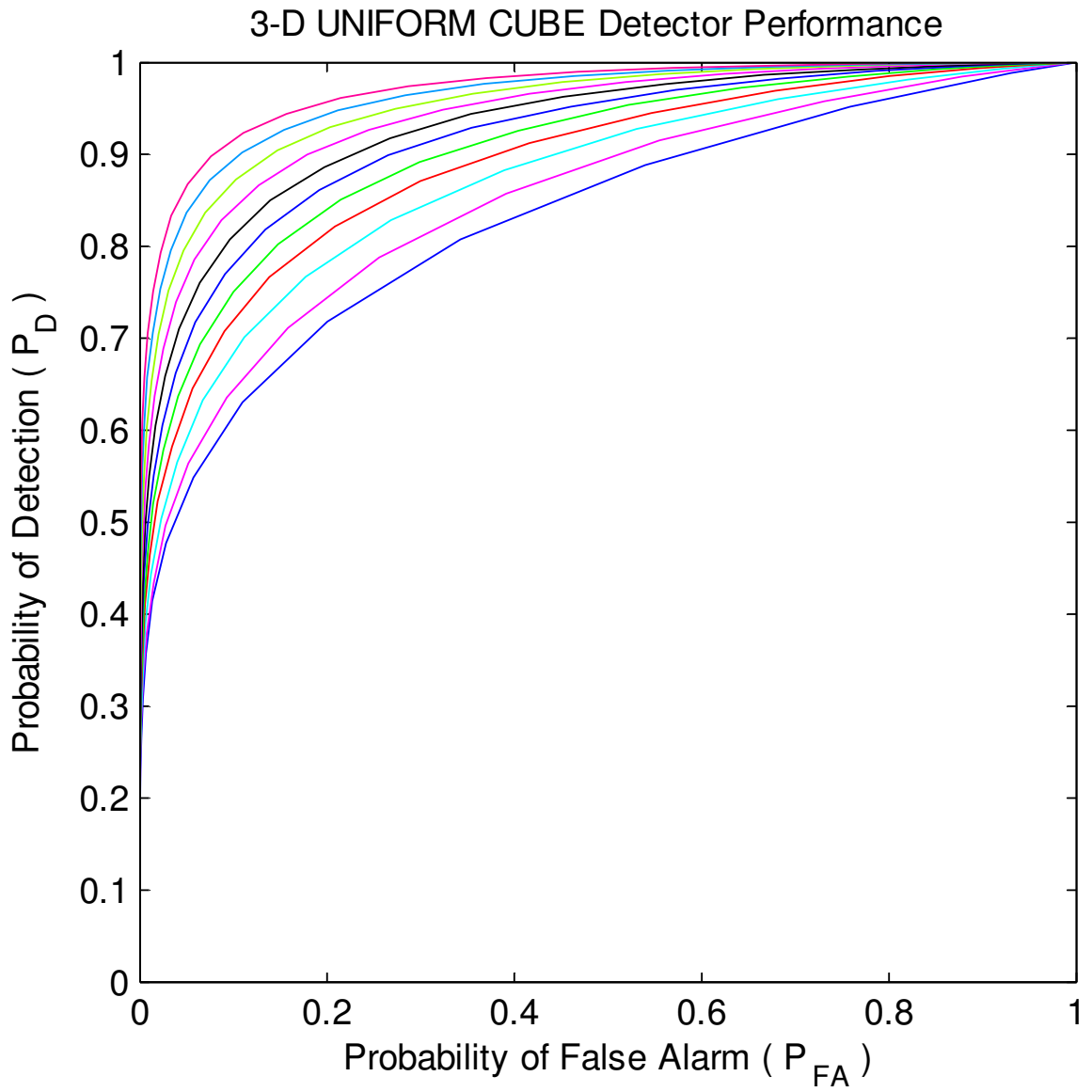
Figure B.5: ROC plot for 3-D Uniform Cube, for fixed SNR
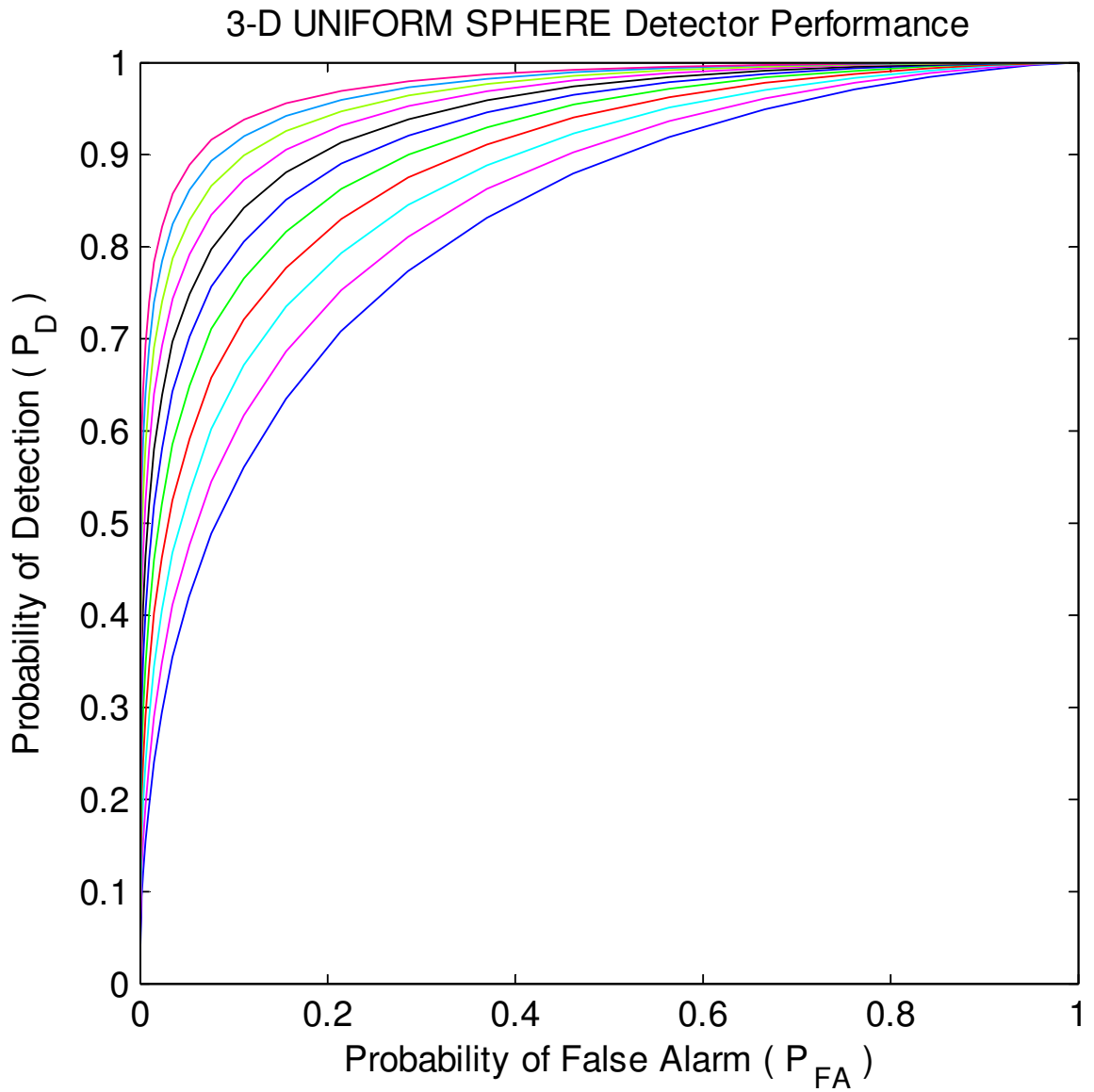
Figure B.6: ROC plot for 3-D Uniform Sphere, for fixed SNR

Appendix C ~ Detector Performance 2

Kullback–Leibler divergence against SNR, for fixed target size
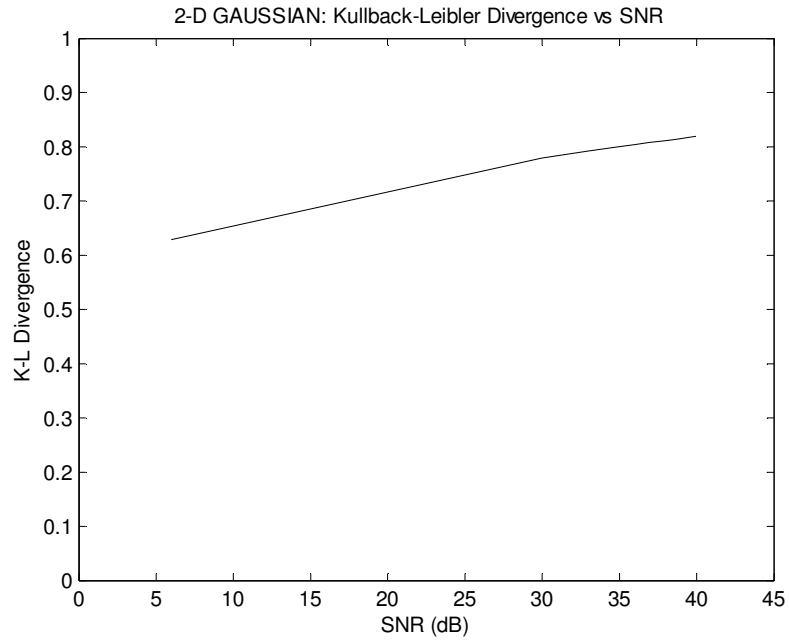
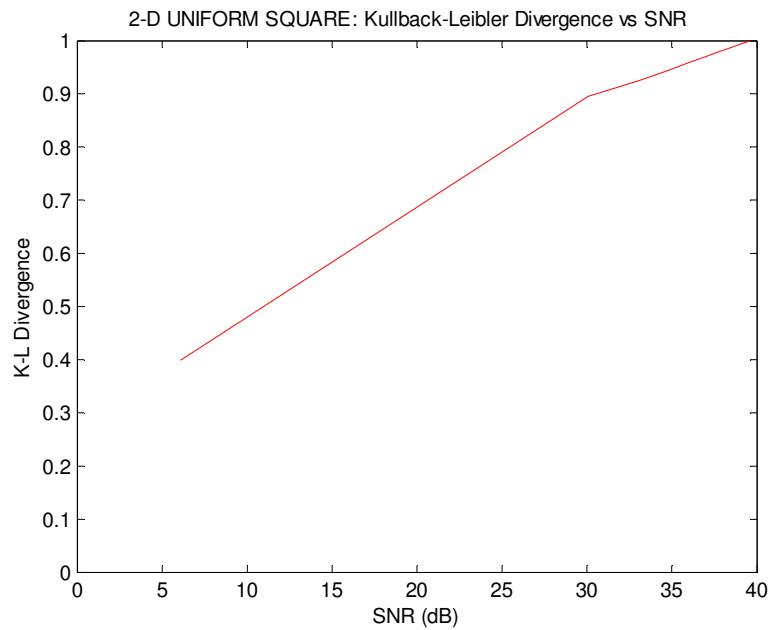Figure C.1: KL divergence of 2-D Gaussian, for fixed Target Size

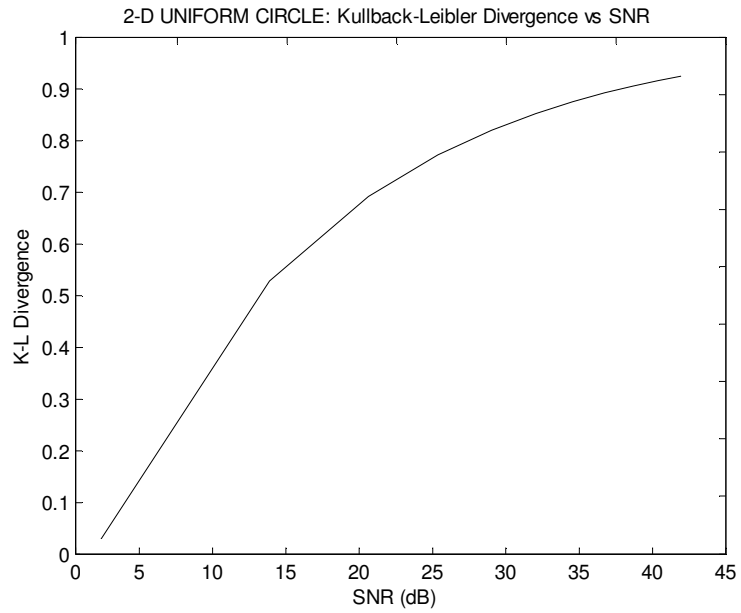Figure C.2: KL divergence of 2-D Uniform Square, for fixed Target Size

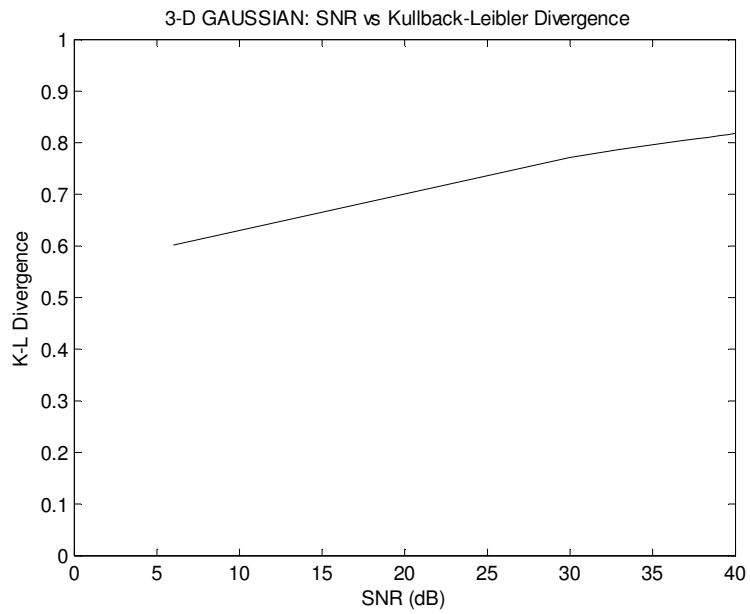Figure C.3: KL divergence of 2-D Uniform Circle, for fixed Target Size

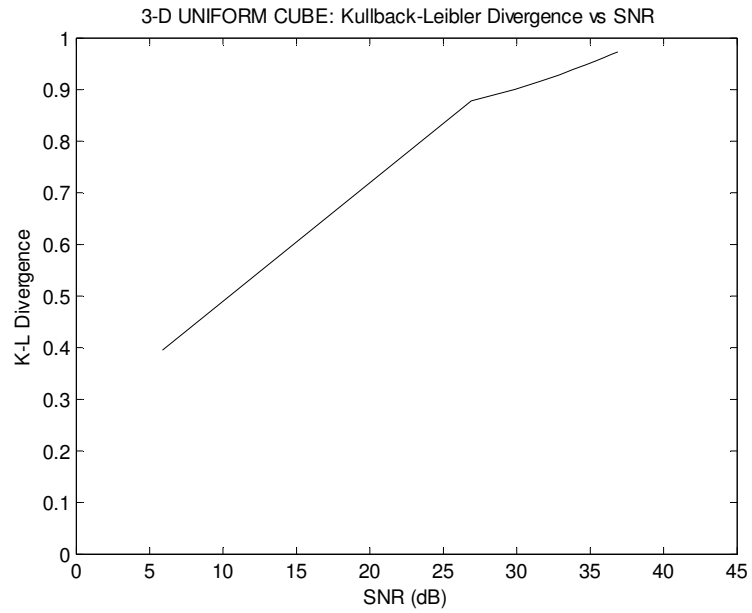Figure C.4: KL divergence of 3-D Gaussian, for fixed Target Size

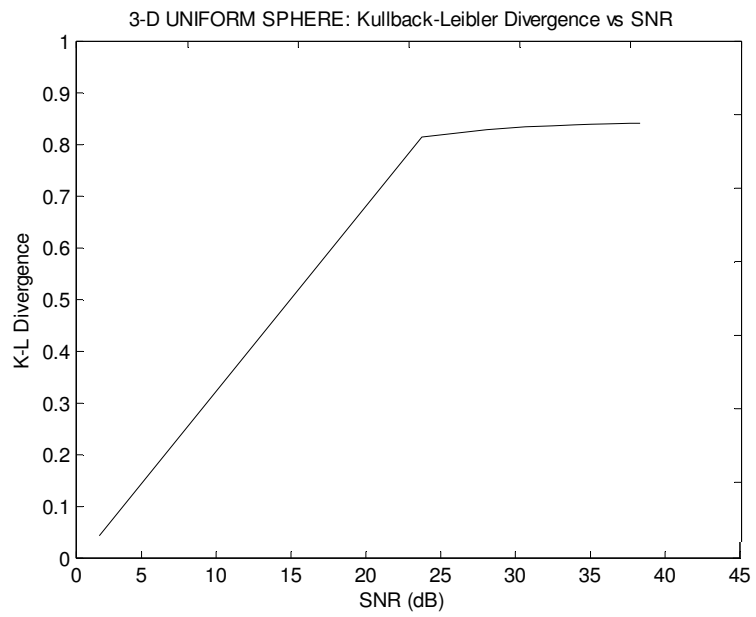Figure C.5: KL divergence of 3-D Uniform Cube, for fixed Target Size

Figure C.6: KL divergence of 3-D Uniform Sphere, for fixed Target Size